Revisiting Jahn–Teller Transitions in Correlated Oxides with Monte Carlo Modeling

Liam A. V. Nagle-Cocco,[1,*] Andrew L. Goodwin,[2] Clare P. Grey,[3] and Siân E. Dutton[4]

[1] *Stanford Synchrotron Radiation Lightsource, SLAC National Accelerator Laboratory, Menlo Park, California, 94025, United States of America*

[2] *Inorganic Chemistry Laboratory, Department of Chemistry, University of Oxford, Oxford, OX1 3QR, United Kingdom.*

[3] *Yusuf Hamied Department of Chemistry, University of Cambridge, Cambridge, CB2 1EW, United Kingdom.*

[4] *Cavendish Laboratory, University of Cambridge, JJ Thomson Avenue, Cambridge, CB3 0US, United Kingdom.*

(Dated: January 15, 2026)

arXiv:2601.09705v1 [cond-mat.str-el] 14 Jan 2026

Jahn–Teller (JT) distortions are a key driver of physical properties in many correlated oxide materials. Cooperative JT distortions, in which long-range orbital order reduces the symmetry of the average structure macroscopically, are common in JT-distorted materials at low temperatures. This long-range order will often melt on heating, *via* a transition to a high-temperature state without long-range orbital order. The nature of this transition has been observed to vary with different materials depending on crystal structure; in $LaMnO_3$ the transition has generally been interpreted as order-disorder, whereas in layered nickelates $ANiO_2$ (A=Li,Na) there is a displacive transition. Alternatively, recent theoretical work has suggested that previous attributions of order-disorder may in fact be a consequence of phonon anharmonicity, rather than persistence of JT distortions, which would suggest that the displacive transition may be more common than currently believed. In this work, we run Monte Carlo simulations with a simple Hamiltonian which is modified to include terms dependent on the JT amplitude ρ, which is allowed to vary within the simulation *via* the Metropolis algorithm. Our simulations yield distributions of JT amplitudes consistent with displacive rather than order-disorder behaviour for both perovskites and layered nickelates, suggesting that displacive-like JT transitions may be more common than previously assumed in both perovskites and layered nickelates. We also find significant differences between the transition observed for perovskites compared with layered nickelates, which we attribute to differing extensivity of configurational entropy on the two lattices, showing the crucial role of lattice geometry in determining behaviour.

I. INTRODUCTION

Transition metal oxide octahedra with electronic configurational degeneracy are susceptible to a Jahn–Teller (JT) distortion[1–7], causing their shape to deviate from that of a regular octahedron. Such distortions most commonly manifest as a linear superposition of the $E_g(Q_2, Q_3)$ van Vleck modes[8,9], where Q_2 and Q_3 are planar rhombic and tetragonal distortions, respectively, although the tetragonal Q_3 component tends to dominate. JT distortions have been observed in both molecules[6] and crystals[7]. The JT distortion, and associated orbital ordering, is relevant to many phenomena including superconductivity in the cuprates[10–12], spin-orbit ordering[13], and ionic mobility[14,15], and can lead to structural transitions on cycling in battery electrode materials[14–16].

Within solids, the axes of octahedral elongation can correlate *via* orbital ordering over macroscopic length-scales as a cooperative JT (cJT) distortion, typically manifesting as a reduction in unit cell symmetry[5,7]. For instance, the perovskites KMF_3 (M=Cr,Cu)[17,18], $LaMnO_3$[19], and $[(CH_3)_2NH_2]Cu(HCOO)_3$[20] exhibit a cJT distortion with alternating MO_6 (M=Cu,Cr,V,Mn) octahedra elongated along two orthogonal directions within the xy-plane, as shown in Figure 1(a). This ordering is generally stacked identically along the c-direction[17,19,21,22]. Interestingly, similar orbital ordering driven by t_{2g} orbitals is seen in the vanadate perovskites AVO_3 (A=Ho,La,Y)[21–24], although on cooling to low temperatures, some (such as $LaVO_3$ and YVO_3) have been shown to exhibit out-of-phase stacking along the c-direction[23–25] [SI Figure S1]. The flexibility of the perovskite structure means that other kinds of ordering can also be exhibited; $Ba_{0.5}La_{0.5}CoO_3$ exhibits a collinear elongational cJT ordering of the CoO_6 octahedra when the La/Ba is disordered[26] but a compressive collinear ordering when the La/Ba is ordered[27] [Figure S2].

cJT distortions also occur in the layered triangular-lattice nickelates $NaNiO_2$[28,30–35] and defect-free $LiNiO_2$[29,36]. Most evidence indicates this is a collinear cJT distortion, where NiO_6 octahedra within each layer all elongate along the same axis and this axis is preserved from layer to layer (shown in Figure 1(b)), although there is some evidence for zigzag-type intra-layer ordering in $LiNiO_2$[36–38] [Figure S3]. Conversely, some orbitally-degenerate nickelates such as $AgNiO_2$[39,40] or the nickelate perovskites[41–43] do not feature JT-distortions, but instead break degeneracy *via* charge disproportionation. There is some computational[38,44,45] and experimental[45–47] evidence for a similar charge disproportionation mechanism, as an alternative to JT behaviour, occurring in $LiNiO_2$.

Beyond perovskites and layered nickelates, JT-driven orbital order occurs in a range of other materials. The K_2PtCl_6-type material $(NO)_2VCl_6$, which has a compressive, not elongational, distortion, exhibits a collinear cJT distortion within the ab-plane,

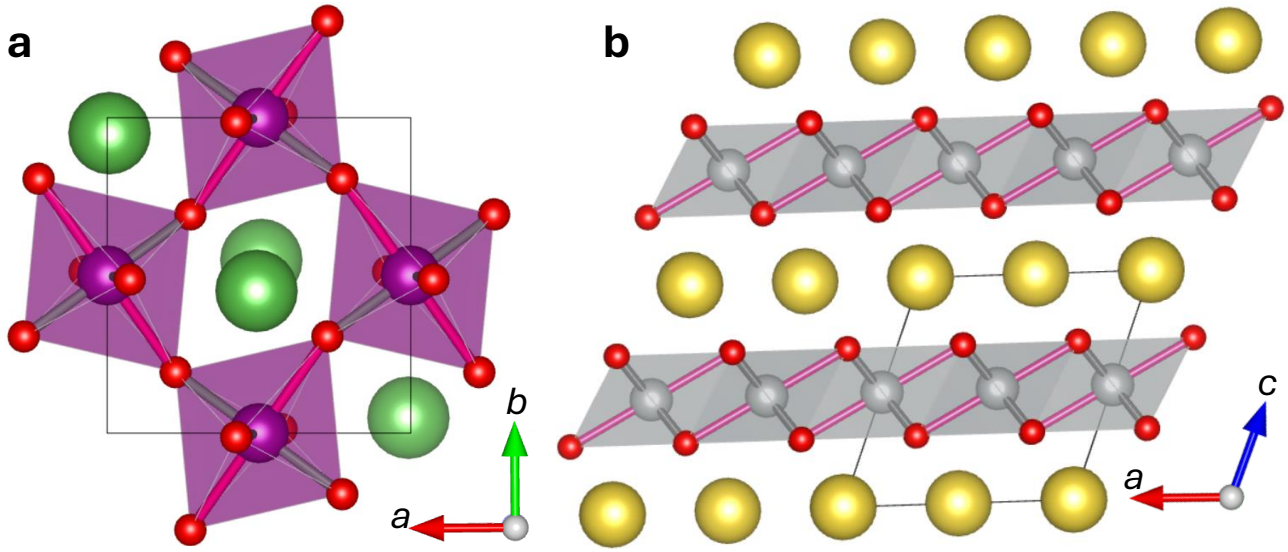

FIG. 1: The room-temperature crystal structures and JT-ordering of (a) many JT-ordered perovskites such as $KCuF_3$ and $LaMnO_3$[13] and (b) layered nickelates such as $NaNiO_2$ and stoichiometric $LiNiO_2$[28,29]. Pink metal-oxygen bond lengths indicate JT-elongated bonds. Only octahedra associated with JT-active sites are displayed. In the perovskites, purple sites are the JT-distorted site (i.e. Mn, Cu, Cr) and green sites are the A-site (i.e. La, K). In the nickelates, grey sites are Ni^{3+} and yellow sites are the alkali metal.

but the axis of octahedral compression alternates with layer stacking[48]. The spinels Mn_3O_4[49], $LiMn_2O_4$[50], $MgMn_2O_4$[51], and $ZnMn_2O_4$[52][Figure S4], wolframite $CuWO_4$[53], Prussian Blue analogs such as $CuPt(CN)_6$[54] and $K_2Cu[Fe(CN)_6]$[55], and Ruddlesden–Poppers like A_2CuF_4 (A=Na,K)[56,57], all exhibit simple collinear cJT distortions, although a pressure-induced change in cJT ordering has been observed in Na_2CuF_4[57]. The distorted trirutile $CuSb_2O_6$[58] also exhibits intra-planar collinear ordering, but alternating ab-planes exhibit different axes of elongation. There are clearly a wide range of possible orbital orderings which may be energetically favourable, depending on the geometry of the octahedral interactions and the JT-active cation.

Heating materials with a cJT distortion will often result in a symmetry-raising transition. In many perovskites, an order-disorder transition has been reported, in which JT distortions persist locally in octahedra even when cJT distortions are suppressed. For example, the canonical orbital-ordered material $LaMnO_3$ shows the melting of long-range orbital order around $T_{JT} \approx 750\,K$[59–71]. Local structure probes such as neutron total scattering[62,68] and extended x-ray absorption fine structure (EXAFS)[65] have typically been interpreted as showing that distortions persist locally within octahedra, and correlate over short lengthscales, although a recent study has indicated these experimental results may actually be consistent with a more complex high-temperature state without conventionally JT-distorted octahedra[72]. An order-disorder transition for $Y_{1-x}La_xVO_3$ has also been reported based on neutron total scattering[73] for all values of x in the range $0 \leq x \leq 0.3$. $KCrF_3$ shows a similar transition in crystal symmetry below $\sim$973 K[74], which is likewise proposed to be order-disorder[74] by analogy to $LaMnO_3$. Surprisingly, the isostructural $KCuF_3$ shows no sign of the melting of orbital order below its decomposition temperature[75].

Besides perovskites, there are reports of order-disorder transitions in other systems too. The spinel $LiMn_2O_4$, although a complex case due to mixed-valence Mn, exhibits a subtle tetragonal→cubic JT transition which appears to be order-disorder based on Mn K edge X-ray absorption spectroscopy[50]. Electron spin resonance measurements on $CuSb_2O_6$ indicate persistence of local JT distortions through the JT transition[76] suggesting an order-disorder transition.

cJT distortions are generally suppressed due to the additional thermal energy in the system[5]. Expansion of the crystal lattice weakens the effective interaction between local JT centers mediating cooperativity, reducing the enthalpy gain associated with orbital ordering. Increasing thermal energy also enables octahedra to dynamically cycle through axes of elongation corresponding to different local energy minima, which would suppress a time-averaged cJT distortion *via* a dynamic JT fluctuation[77]. Additionally, free energy becomes dominated by entropic contributions over enthalpic contributions on heating, and so enthalpy minimisation due to cJT will be less of a factor in determining the crystal structure[78]; this is important as there may be significant configurational entropy associated with orbital disorder depending on the geometry of the lattice in question[34]. An interpretation of JT transitions as order-disorder can therefore be explained in terms of maximising configurational entropy

at high temperature.

Layered nickelates $LiNiO_2$ and $NaNiO_2$ are promising battery materials[81–84], and so the nature of the JT transition in these materials has attracted much interest[29,33–35,85,86]. Computational work based on Monte Carlo simulations integrated with density functional theory (DFT)[85] concluded that although the parameter phase space for layered nickelates can accommodate both an order-disorder and a displacive transition, an order-disorder transition is more likely in common with previously-studied JT transitions.[85] However, more recently, both experimental[34,87] and *ab initio* molecular dynamics simulations[34,86] have indicated that layered nickelates exceptionally exhibit displacive JT transitions, in which there is no minimum in the free energy landscape associated with JT distortions above the JT transition. This was attributed[34] to the subextensive configurational entropy associated with orbital disorder on a 2D triangular lattice in which the axes of elongation are geometrically constrained by the chemical instability associated with having multiple axes of elongation pointing at a common O anion. In contrast, we note that evidence for an order-disorder transition in non-stoichiometric $LiNiO_2$ with site-mixing has also been reported[87].

While the observation of displacive behaviour in nickelates appeared exceptional at the time they were reported, a recent study[72] has shown that experimental data for the $LaMnO_3$ case can be reproduced without well-defined and prevalent octahedral elongations. This would indicate that dynamics, rather than configurational entropy, is the key driver of behaviour through JT transitions. Further, it would indicate that displacive JT transitions may be more common, or even ubiquitous if a paradigm shift in our perspective JT transitions were to follow. This justifies close scrutiny of the evidence for previous assignments of order-disorder character to JT transitions.

The cJT distortion in perovskites was previously studied in Monte Carlo simulations by Ahmed and Gehring (2005)[78] and applied to the case of $LaMnO_3$[79,80]. In their model, an anisotropic Potts variable on each site successfully reproduced the cJT ordering at room-temperature in $LaMnO_3$[78,79] and the dependence of lattice parameters on temperature through the JT transition[80]. However, their simple model did not include amplitudes of JT distortion or the possibility of JT-undistorted MnO_6 octahedra, and so an order-disorder transition was implicitly built into the model. More recently, Tragheim *et al.* (2025)[71] developed a more complex model in which JT amplitude may vary as a consequence of the octahedral tilts and shapes, which are the varying parameters; however, they do not apply this directly to the temperature-induced JT transition.

For the layered nickelates, Radin *et al.*[85] used an anharmonic vibrational Hamiltonian with continuous JT modes and Monte Carlo sampling, parametrized from DFT. Unlike the model of Ahmed and Gehring, this more complex approach[85] contains a regime in the phase space of starting parameters, the stiff-lattice regime, which can lead to displacive behaviour. However, using parameters from DFT, they predicted that layered nickelates would occur in the soft-lattive regime where order-disorder transitions are predicted by the Monte Carlo simulations.

In this present work, we extend the relatively simple model of Ahmed and Gehring with variable amplitude, ρ, of JT distortion on each site and a single-ion term in the Hamiltonian to simulate the enthalpy saving associated with JT distortion. Using this model, we simulate the JT transitions in perovskites such as $LaMnO_3$. We then develop a very similar, simple model for the layered nickelates.

We find that the mean magnitude of JT distortion decreases through the transition but remains non-zero, with the high-temperature magnitude being larger in the perovskite lattice than the 2D nickelate lattice, consistent with experimental results which are interpreted in terms of an order-disorder transition. However, the distribution of values of JT magnitude does not resemble that at low-temperatures. For an order-disorder transition, we would expect to see a well-defined peak in the distribution at finite, non-zero ρ, with negligible density at $\rho = 0$. Instead, we see little preference for any particular ρ value at high-temperatures, which appears consistent with dynamic exploration of the $E_g(Q_2,Q_3)$ phase space. Our findings therefore support the reinterpretation of prior reports of order-disorder JT transitions first suggested by Batnaran *et al.*[72], and suggest that displacive JT transitions may be more common than previously thought.

II. METHODOLOGY

A. Hamiltonian

We define a global classical, non-quantum Hamiltonian, for a system with N JT-active octahedra, as follows:

$$H = E_{\mathrm{single-ion}} + E_{\mathrm{geometry}} \tag{1}$$

1. *Single-ion term*

In this Hamiltonian, $E_{\mathrm{single-ion}}$ is the enthalpic impetus to JT distortion. It is defined following a Landau-like second-order expansion of the free energy[5] thus:

$$E_{\mathrm{single-ion}} = \sum_{i}^{N} \left[\alpha\rho_i^2 + \beta\rho_i^4\right] \tag{2}$$

in which ρ_i is the magnitude of the JT distortion at the ith JT-active site. α and β are empirical parameters which determine the functional dependence of enthalpy on ρ. Typically, we would expect $\alpha < 0$, $\beta > 0$, and $|\beta| < |\alpha|$.

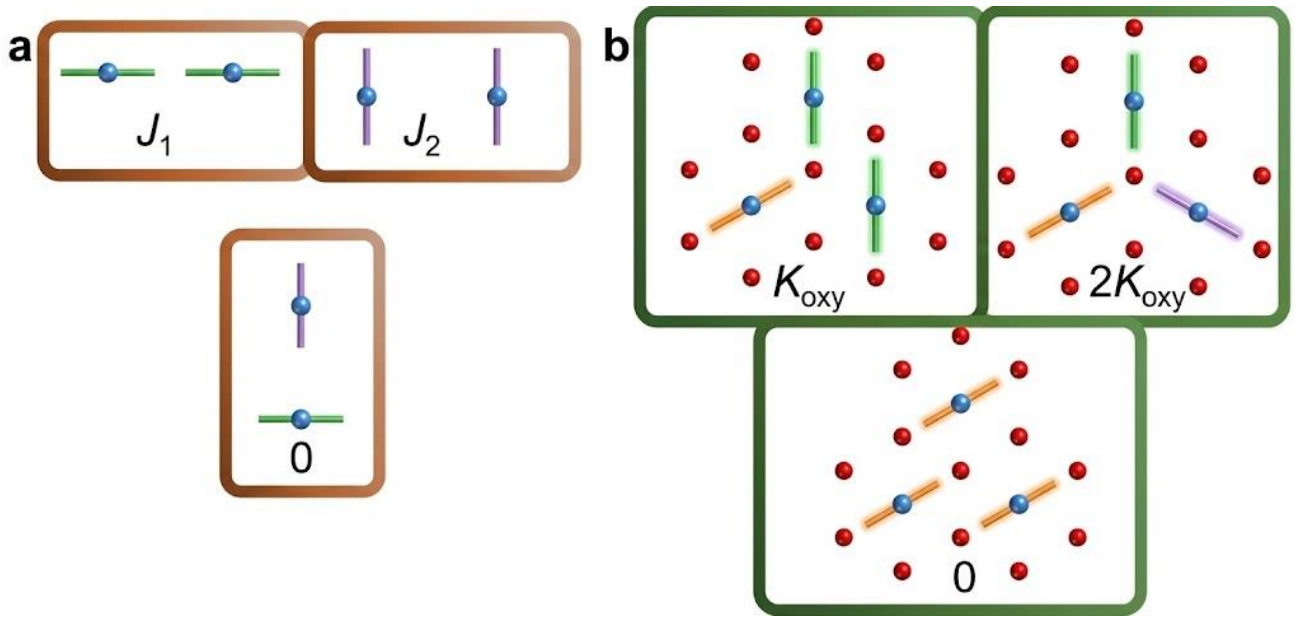

FIG. 2: Diagram showing the JT configurations associated with zero and non-zero geometric energies as used in Equations 3 and 5. (a) The case for perovskites, which is a reproduction of the Potts model of Ahmed and Gehring[78–80]. (b) The case for intra-layer nearest-neighbour NiO_6 octahedra within layered nickelates. Blue solid circles indicate JT-active sites, red solid circles (for the layered nickelate case) indicate O atoms, and solid lines indicate JT elongations.

2. *Geometry term*

The E_{geometry} term is defined uniquely based on the structure in question. For the case of perovskites, this E_{geometry} term is equivalent to the anisotropic Potts model Hamiltonian defined by Ahmed and Gehring[78–80], reproduced as follows over all nearest-neighbour JT-active pairs i, j:

$$E_{\text{geometry}}^{\text{perovskite}} = \frac{1}{2} \sum_{\langle i,j \rangle} w(\rho_i, \rho_j)\, J_{S_i}(\hat{\mathbf{e}}_{ij})\, \delta_{S_i,S_j}, \qquad (3)$$

In this equation, S_i is the direction of octahedral elongation at JT-active B-site cation i, representing the orbital state of the JT-active B-site cation; it can take one of three possible values. δ_{S_i,S_j} is the Kronecker delta which enforces that only like-orbital pairs contribute to the interaction energy. $\hat{\mathbf{e}}_{ij}$ is the unit vector pointing from site i toward site j. $J_{S_i}(\hat{\mathbf{e}}_{ij})$ is the anisotropic interaction constant, which takes a value J_1 if the direction of $S_i = S_j$ matches $\hat{\mathbf{e}}_{ij}$ and a value of J_2 otherwise, as shown in Figure 2(a). The prefactor $\frac{1}{2}$ avoids double counting of site pairs in the nearest-neighbor sum $\langle i, j \rangle$.

The multiplier $w(\rho_i, \rho_j)$ is used in this case to reduce the contribution to the geometry term of undistorted octahedra without incentivising infinite distortion. It is defined thus:

$$w(\rho_i, \rho_j) = 2\rho_i\rho_j/(1 + \rho_i\rho_j) \qquad (4)$$

The possible values of $J_{S_i}(\hat{\mathbf{e}}_{ij})$, J_1 and J_2, are empirical constants, the values of which will determine the ground-state cJT ordering. Ahmed and Gehring found that[79] the cJT in room-temperature $LaMnO_3$ is reproduced by $J_1 > 0$, $J_2 < 0$, and $|J_2/J_1| < 1/2$. The collinear JT ordering found, for instance, in $Ba_{0.5}La_{0.5}CoO_3$[26] could be reproduced for $J_2 < 0$ and $J_1 < -J_2$.

For the layered nickelates, the geometric energy term is based on the chemical instability associated with underbonding of O anions. For instance, an earlier work[36] proposed a trimer-like cJT ordering in $LiNiO_2$ in which three elongated Ni-O bonds point at the same oxygen anion, but subsequent computational studies using DFT[37] showed this to be highly unstable relative to collinear or zigzag models in which a single elongated bond points at each oxygen anion. We calculate this by summing over all O anions in the simulation as follows:

$$E_{\text{geometry}}^{\text{nickelate}} = \frac{K_{\text{oxy}}}{2} \sum_{O} \left[\max\left(0,\ s_O - 1\right)\right]^2 \qquad (5)$$

where K_{oxy} is an empirical parameter, $K_{\text{oxy}} > 0$, which determines the strength of this O under-bonding penalty, with the implication of this equation shown in Figure 2(b). The "underbonding density" term s_O is given by summing over all three nearest-neighbour Ni cations to a given O anion thus:

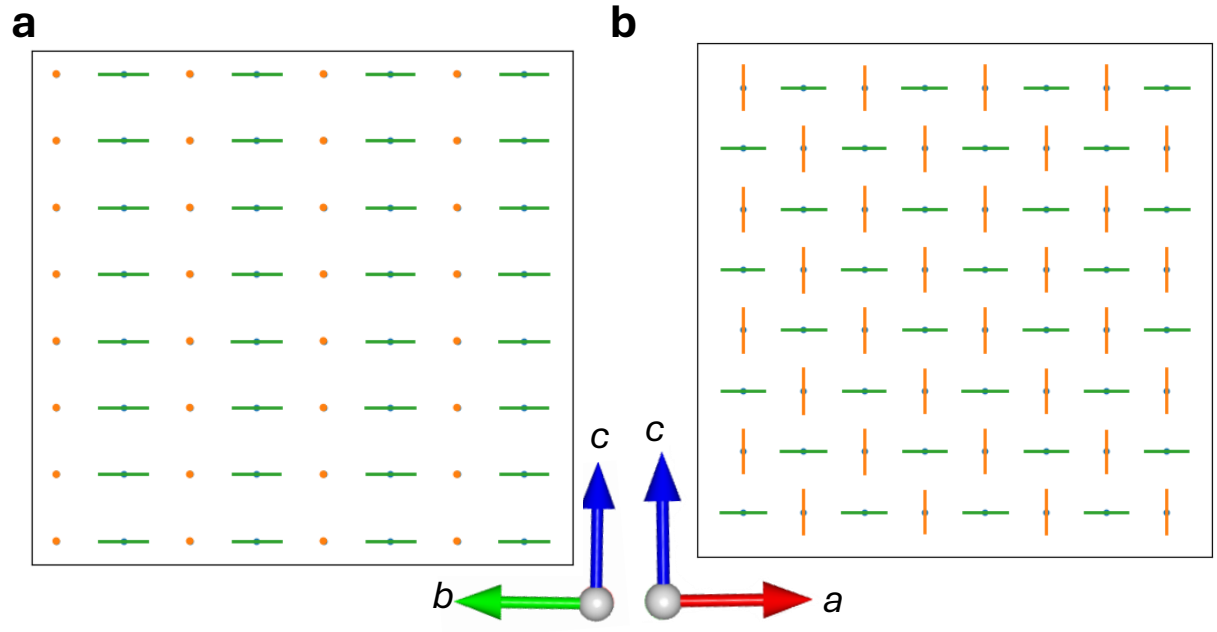

FIG. 3: The results of a Monte Carlo refinement with dynamic ρ ($p_{\text{switch}} = 1/2$), reproducing Phase 5 (C-type) of the Ahmed and Gehring[78] phase diagram for the anisotropic Potts model in a $8 \times 8 \times 8$ perovskite supercell. (a) Example configuration in the *bc*-plane in a randomly-selected cross-section. (b) Example configuration in the *ac*-plane in a randomly-selected cross-section. Energy parameters $\alpha = -1, \beta = 1/2$ from equation 1. Simulated annealing was used before settling on a final $T = 0.001$. This run lasted for 10^7 iterations. Plots of energy and $\langle\rho\rangle$ with iteration can be seen in Figure S12.

$$s_O = \sum_{i \in N(O)} \delta_{\vec{\rho}_i, \vec{r}_{iO}} \, \rho_i, \tag{6}$$

where $\delta_{\vec{\rho}_i, \vec{r}_{iO}}$ is 0 or 1 depending on whether the elongated Ni-O bond ($\vec{\rho}_i$) matches the vector between the Ni and the O anion ($\vec{r}_{iO}$).

We note that the nature of the Hamiltonian we use here renders us insensitive to the possibility of disproportionation as proposed in some prior works[38,44,45].

The perovskite and nickelate E_{geometry} term share the same degrees of freedom (a three-state elongation axis and a continuous amplitude ρ), but differ qualitatively in their interaction terms: pairwise orbital alignment in the perovskite case, versus oxygen-underbonding constraints in the nickelate case. Consequently, the nickelate geometry term is no longer a Potts Hamiltonian as the perovskite geometry term is.

B. Model cell

Simulations are run over periodic cells in two- or three-dimensions for the layered nickelate and perovskite case, respectively. For the perovskite case, a cubic primitive cell is used with a $8 \times 8 \times 8$ grid of metal cations (512 atoms). For the layered nickelate case, the cell is a 10×30 rhombus-shaped grid of Ni cations (300 atoms), where the two basis vectors enclose 60°. The use of a two-dimensional lattice relies on the axiom that inter-layer interactions are not significant for the JT ordering. Unless otherwise indicated, the starting configuration for all runs was one in which JT distortions were randomly distributed within the unit cell, all with identical magnitude $\rho = 1$.

C. Metropolis algorithm

The Monte Carlo simulation runs over a number of iterations (10^5 to 10^7) using the Metropolis algorithm[88]. At each iteration, a metal site is selected at random. With probability $0 \leq p_{\text{switch}} \leq 1$, a ρ shift occurs in which the magnitude of ρ is varied randomly by some amount, with $-0.1 \leq \Delta\rho \leq 0.1$ (with ρ capped at 0 at the lower limit and 1.5 at the upper limit). Alternatively, a direction shift occurs, in which the axis of elongation of the metal site is shifted randomly. Energy is then re-calculated according to Equation 1. If $\Delta E \leq 0$, the change is accepted. Otherwise, the change is accepted with probability $\exp[-\Delta E/T]$. For most testing in this work, p_{switch} was set arbitrarily at 0.5.

Where indicated, a simulated annealing procedure is used to avoid being stuck in local minima. This is discussed in Appendix A.

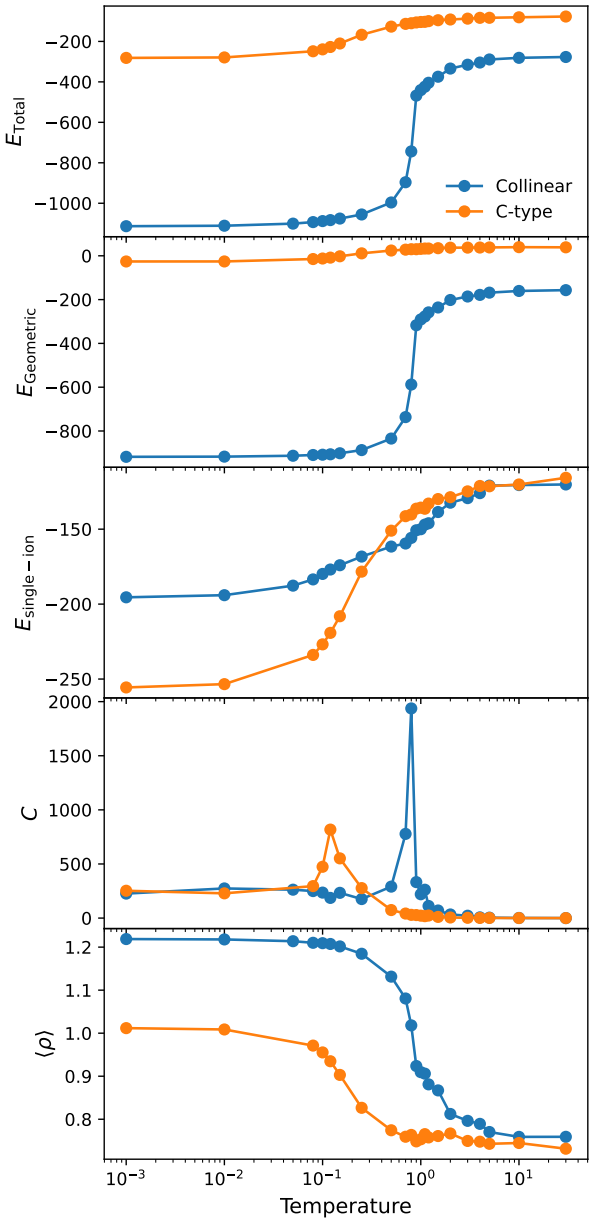

FIG. 4: The mean energy terms E_{total}, $E_{\text{Geometric}}$ (Eq 3), and $E_{\text{single-ion}}$ (Eq 2), heat capacity C, and mean $\langle\rho\rangle$, averaged over the final 10% of iterations in Monte Carlo simulations, as a function of temperature for the collinear and C-type orbital orderings in a $8 \times 8 \times 8$ perovskite lattice. The Monte Carlo simulations ran for 10^7 iterations in total at each temperature. This figure is reproduced on a non-logarithmic temperature scale in SI Figure S13.

III. RESULTS: JT-DISTORTED PEROVSKITE

Before allowing ρ to vary (i.e. by setting all metal sites to have constant non-zero JT magnitude, and setting $p_{\text{switch}} = 0$), we tested our model where the Hamiltonian consisted of the $E^{\text{perovskite}}_{\text{geometry}}$ term only (i.e. $\alpha = \beta = 0$), as shown in SI Section S2. This reproduced the (J_1, J_2) anisotropic Potts model phase diagram of Ahmed and Gehring[78], validating their results and our simulation approach.

Two phases of the Ahmed and Gehring phase diagram are of particular interest which we call "collinear" and "C-type" (phase 1 and phase 5 using Ahmed and Gehring's notation). Collinear is a ferro-orbital model with parallel axes of elongation, and C-type consists of alternating stacked elongations within a single plane [Figure 1(a)]. These are of interest because they have been reported experimentally. We henceforth only study these two phases for perovskites. The next step was to test whether, for $T << 1$, adding a dynamic JT magnitude with the $E_{\text{single-ion}}$ term enables the recovery of these two phases.

Figure 3 shows the energy and mean JT magnitude $\langle\rho\rangle$, along with some cross-sections of the final perovskite supercell for the "C-type" ordering (where $J_1 = 1$ and $J_2 = -0.1$), indicating successful convergence with the expected orbital order. Figure S11 shows the corresponding information for the collinear case. In both cases, the dynamic ρ model is able to reproduce the phase diagram given by the static ρ model[78].

We next consider the variable-temperature behaviour of these orbital orderings. We performed simulations, with simulated annealing, at a series of temperatures up to $T = 30$, for both the collinear and C-type (J_1,J_2) configurations. Figure 4 shows the mean energy and $\langle\rho\rangle$ for the final 10% of iterations in the simulations as a function of temperature, for both cases. We see that, as temperature increases, there is a transition, which can be seen best in the heat capacity data [Figure 4], where heat capacity is the variance in E_{total} divided by T^2. $\langle\rho\rangle$ decreases with heating, with the rate of decrease being low on approach to the transition, and then a rapid decrease before settling at around $\langle\rho\rangle \approx 0.8$. We have tested the resilience of this finding against varying cell size [Figures S16 and S17] with little variation. The finding that $\langle\rho\rangle$ decreases on heating even in the low-temperature regime approximately corresponds to experimental observations from diffraction on $LaMnO_3$, although $KCuF_3$ exhibits the opposite trend[75].

A convergence of $\langle\rho\rangle \to 0.8$ at high temperatures appears consistent with the experimental reports (from PDF and EXAFS) of JT-like octahedral distortion at high-temperatures, if we interpret it as the system remaining in the enthalpic minimum imposed by Eq 2. However, when we plot histograms of ρ in the final configuration [Figure 5], we see that the distribution at high temperature does not resemble the distribution at low temperature, which would be the signature of an order-disorder transition. Instead, we see $N(\rho)$ appears invariant with the magnitude, which suggests that rather than a persistence of JT distortions the system is merely dynamically exploring the available phase space of possible values of ρ, which is consistent with the recent theoretical study of $LaMnO_3$[72]. These findings could be interpreted

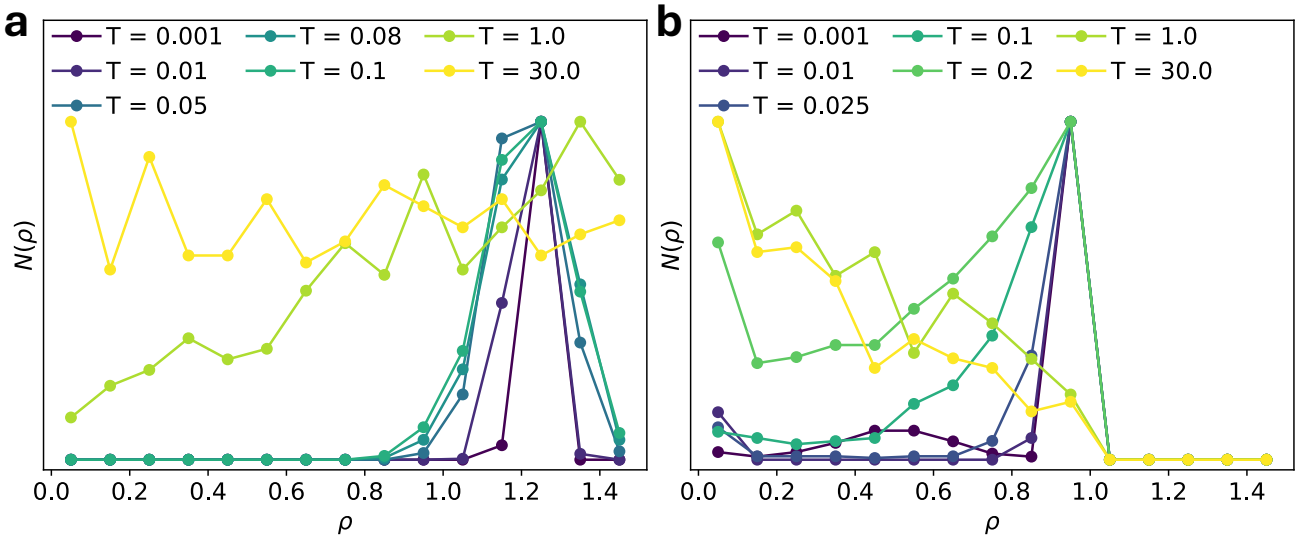

FIG. 5: Histograms of ρ for (a) $8 \times 8 \times 8$ perovskite collinear ordered supercell and (b) the final 10×30 nickelate layer with $K_{\text{oxy}} = 10^{10}$ after 10^7 iterations, with simulated annealing. For other configurations see Figures S18 to S22.

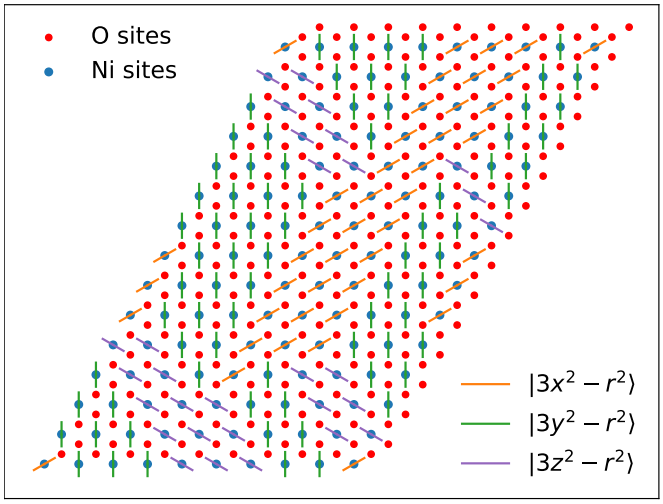

FIG. 6: An example converged configuration of a 10×15 layered nickelate. This simulation used a static ρ ($p_\rho = 0$; $\alpha = \beta = 0$) model, with $K_{\text{oxy}} = 10^{10}$ and $T = 0.001$ after simulated annealing (with $T_{\text{max}} = 10$), and was run for 10^6 iterations. Collinear domains can be seen, often bound by defects of over-bonded (no JT axes) or under-bonded (multiple JT axes) oxygen anions, indicating that this is a local, but not global, energy minimum. In this simulation, we set $K_{\text{Oxy}} = 10^{10}$.

more in terms of a displacive transition than an order-disorder transition, although the invariance in $N(\rho)$ with ρ indicates that if there is a free energy minimum at the origin in $E_g(Q_2, Q_3)$ phase space, it is not significantly more stable than other regions of the phase space.

IV. RESULTS: LAYERED NICKELATE

We next simulated the layered nickelates. Here, we rely on the axiom that inter-layer effects are negligible due to the AO_6 octahedral layer (A=Li,Na), and consider only single layers. As with the perovskites, we first performed Monte Carlo simulations for the static ρ case where all sites begin JT-distorted, with $p_{\text{switch}} = 0$, and the Hamiltonian consisting solely of the $E^{\text{nickelate}}_{\text{geometry}}$ term (i.e. $\alpha = \beta = 0$), with $T << 1$. An example of a converged layer configuration is shown in Figure 6. We see the emergence of ordered collinear domains, as reported from diffraction studies on $NaNiO_2$[28,30,32,33] and stoichiometric $LiNiO_2$[29]. The boundary between these domains resembles the "zigzag" ordering which has been proposed as a possible ground state for $LiNiO_2$ on the basis of DFT studies[37,38]. Defects then occur when two or three domains intersect. Such defects involve either over-bonded (no JT axes) or under-bonded (multiple JT axes) oxygen anions, and resemble the dimer or even trimer models proposed by Chung *et al* (2005)[36] [Figure S1] which have been found from DFT to be highly unstable[37]. This domain effect, in contrast, does not seem to be important for the perovskites, likely because they can relieve frustration by stacking patterns along c, which reduces the likelihood of frustrated interactions.

For $T << 1$, we see this behaviour is preserved when working with the dynamic ρ and non-zero $E_{\text{single-ion}}$ term, with K_{oxy} arbitrarily large (i.e. 10^{10}). From here, we iteratively increase temperature and evaluate the changes in $\langle\rho\rangle$, as shown in Figure 7. As with the perovskites, the heat capacity C shows that an ordering transition occurs, above which there is local disorder. We see that, keeping K_{oxy} arbitrarily large, as $T \to \infty$,

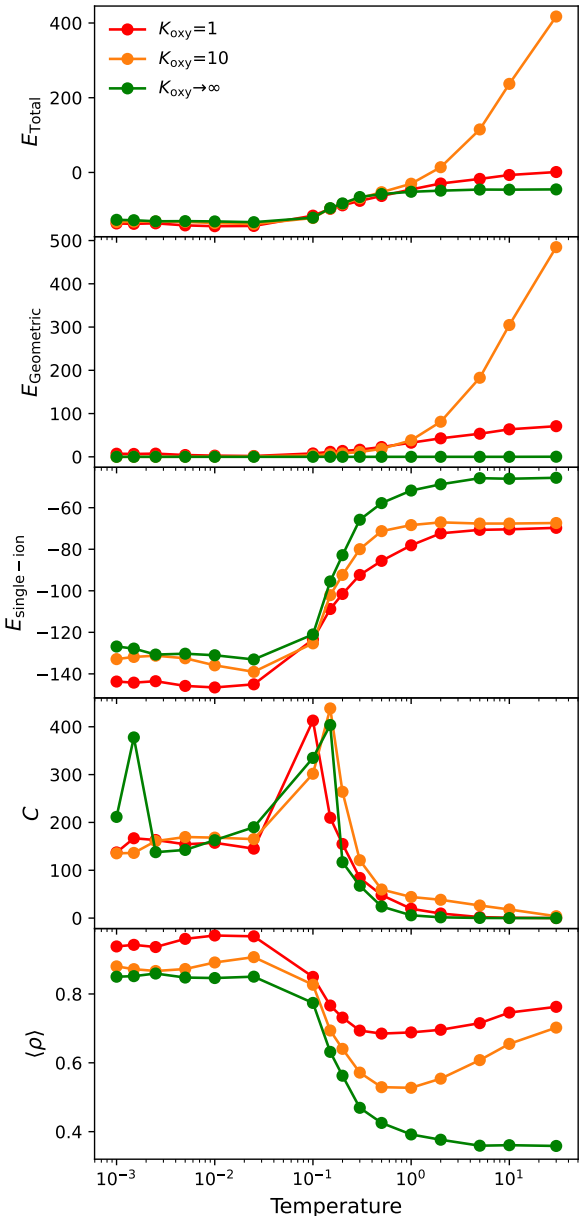

FIG. 7: The mean energy terms E_{total}, $E_{\text{Geometric}}$ (Eq 5), and $E_{\text{single-ion}}$ (Eq 2), heat capacity C, and mean $\langle\rho\rangle$, averaged over the final 10% of iterations in Monte Carlo simulations, as a function of temperature for the 10×30 nickelate lattice. The Monte Carlo simulations ran for 10^7 iterations in total at each temperature. We present these results as a function of the strength of the oxygen under-bonding penalty K_{oxy}. This is plotted on a non-logarithmic temperature scale in Figure S14.

$\langle\rho\rangle \to 0.4$, much lower than the perovskite case. Figure 5 shows histograms of ρ at low and high temperatures, with most Ni sites exhibiting a large JT distortion at low-T (except a few Ni sites which occur at the boundary between domains), and Ni sites at high temperatures exhibiting no preference for JT distortion, with the highest distribution of sites occurring at low-ρ. This suggests that the preference for large ρ and JT distortions vanishes on the 2D nickelate lattice, which is displacive-like behaviour. Although our simulations for the perovskites were broadly consistent with a similar conclusion, there clearly exist differences between these two cases: (1) the significantly reduced $\langle\rho\rangle$ at high T for the nickelate case compared with the perovskite case and (2) the decreasing $N(\rho)$ with ρ for the nickelate case compared with the approximate invariance of $N(\rho)$ with ρ in the perovskite case.

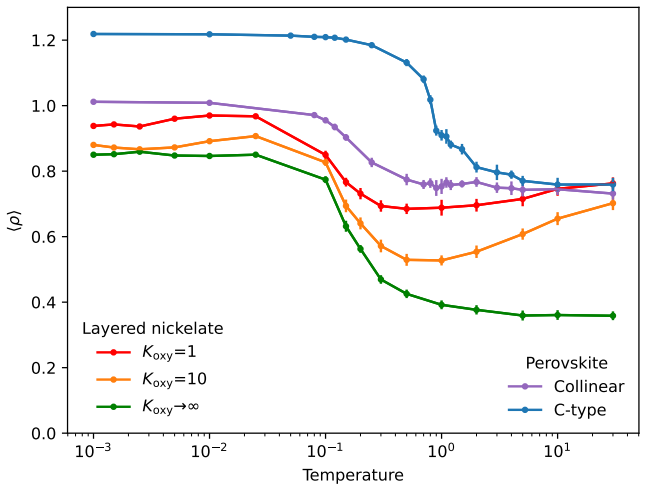

FIG. 8: $\langle\rho\rangle$ with temperature, comparing phase 1 (collinear) and phase 5 (C-type) perovskite ordering with layered nickelates for various K_{oxy}. The corresponding figure with non-logarithmic temperature scaling is Figure S15.

In Ref.[34], we presented a mathematical proof that JT disorder in layered nickelates has subextensive configurational entropy, and argued that this drives the displacive behaviour in layered nickelates. One of the axioms of this proof is that oxygen underbonding is unfeasible and so multiple axes of JT elongation do not point at the same oxygen; this is equivalent to our choice in these Monte Carlo simulations to set $K_{\text{oxy}} \to \infty$. In Figure 7, we also show the temperature-dependence of $\langle\rho\rangle$ if we reduce the magnitude of K_{oxy} (while retaining $K_{\text{oxy}} > 0$), i.e. resulting in scenarios such as the trimer or dimer JT-ordering being energetically unfavourable but not totally unfeasible as for the $K_{\text{oxy}} \to \infty$ case. This results in $\langle\rho\rangle$ converging much higher, similar to the case for the perovskites, indicating order-disorder behaviour. This further supports the notion that preventing O under-bonding, and hence restricting the configurational entropy to be subextensive, is a crucial prerequisite to achieving displacive behaviour in JT-distorted materials.

V. CONCLUSION

In this study, we successfully extended the Monte Carlo model of Ahmed and Gehring[78–80] to include variable Jahn-Teller (JT) distortion amplitudes, enabling us to retain the simplicity of the Ahmed and Gehring model, while allowing for the possibility that JT distortions may vanish locally at high-temperature. The results of this approach are qualitatively consistent with both experimental evidence for persistence of JT-like distortion modes above JT transitions in perovskites[60,62] (which, in our simulations, manifests as a high $\langle\rho\rangle$), and recent computational results which suggest that the high-temperature state of JT-distorted perovskites is not characterised by well-defined JT-distorted octahedra[72], but rather a dynamic sampling of the (Q_2,Q_3) phase space. These findings suggest that a displacive-like transition, such as that recently reported experimentally for the cJT suppression in the layered nickelates[34,86], may in fact be a more accurate description of cJT suppression than the more orthodox order-disorder description.

Despite our interpretation that both the transition in perovskites and layered nickelates may be better described as displacive than order-disorder, there are clearly differences between the two systems due to the geometry of the lattice. We reported that the converged $\langle\rho\rangle$ of the perovskite lattices is much higher ($\sim$0.8) than the nickelate lattice ($\sim$0.4) at high temperature, and as shown in Figure 5 the number distribution of distortion magnitudes appears invariant with ρ for the perovskite case but levels off as ρ increases for the nickelate case. This is likely a consequence of the subextensivity of configurational entropy of disordered octahedral elongations on the nickelate lattice, as previously reported[34]. The differences likely manifest experimentally in a larger peak skewness, for the first metal-oxygen peak in experimental pair distribution function data, for perovskites like $LaMnO_3$ compared with nickelates like $NaNiO_2$. This may be a factor in the historic attribution of order-disorder behaviour to the JT transitions in the perovskites.

Besides the layered nickelates and perovskites studied in this work, the model presented here may be applied to other JT-distorted systems of interest. For instance, spinels, double perovskites, and Prussian Blue analogs all exhibit cJT distortions. Future work should investigate these systems, and benchmark findings against local probe experiments such as total scattering and EXAFS. Additionally, useful future work would apply the more complex anharmonic vibrational Hamiltonian of Radin *et al.*[85] to perovskite systems such as $LaMnO_3$ to better understand the recent developments in our understanding of these systems.

SOFTWARE

Code was written in Python 3[89], with assistance from generative large-language models ChatGPT[90] version 5 and GitHub Copilot. Graphs are prepared using Matplotlib[91]. Crystal structures prepared using VESTA 3[92].

ACKNOWLEDGMENTS

The authors thank James M. A. Steele, Nicola D. Kelly, and Amber Visser at the University of Cambridge, and Annalena R. Genreith-Schriever at RWTH Aachen University, for useful comments.

Appendix A: Simulated annealing

In the simulated annealing procedure, temperature is initialised at $T_0 = \max(T_{\max}, 10 \cdot T_{\text{target}})$ where T_{target} is the target temperature of the run and $T_{\max} >> 1$. At each iteration i out of a total number of iterations n, the temperature T_i is given by:

$$T_{\text{i}} = \begin{cases} T_0 \left(\dfrac{T_{\text{target}}}{T_0} \right)^{\frac{i}{n_{\text{sa}}-1}} & \text{if } i < n_{\text{sa}}, \\ T_{\text{target}} & \text{if } i \geq n_{\text{sa}}. \end{cases} \tag{A1}$$

where $n_{\text{sa}} = 0.8n$ rounded down to the nearest integer.

* lnc@slac.stanford.edu

[1] H. A. Jahn and E. Teller, Proceedings of the Royal Society of London. Series A-Mathematical and Physical Sciences **161**, 220 (1937).
[2] U. Öpik and M. H. L. Pryce, Proceedings of the Royal Society of London. Series A. Mathematical and Physical Sciences **238**, 425 (1957).
[3] H. C. Longuet-Higgins, U. Öpik, M. H. L. Pryce, and R. A. Sack, Proceedings of the Royal Society of London. Series A. Mathematical and Physical Sciences **244**, 1 (1958).
[4] J. Kanamori, Journal of Applied Physics **31**, S14 (1960).
[5] G. A. Gehring and K. A. Gehring, Reports on Progress in Physics **38**, 1 (1975).
[6] M. A. Halcrow, Chemical Society Reviews **42**, 1784 (2013).
[7] J. B. Goodenough, Annual Review of Materials Science **28**, 1 (1998).
[8] J. H. Van Vleck, The Journal of Chemical Physics **7**, 72 (1939).
[9] L. A. V. Nagle-Cocco and S. E. Dutton, Journal of Applied Crystallography **57**, 20 (2024).
[10] D. V. Fil, O. I. Tokar, A. L. Shelankov, and W. Weber, Physical Review B **45**, 5633 (1992).
[11] H. Keller, A. Bussmann-Holder, and K. A. Müller, Materials Today **11**, 38 (2008).
[12] A. Bussmann-Holder and H. Keller, Condensed Matter **7**, 10 (2022).

[13] D. I. Khomskii and S. V. Streltsov, Chemical Reviews **121**, 2992 (2021).
[14] H. Kim, G. Yoon, I. Park, K. Y. Park, B. Lee, J. Kim, Y. U. Park, S. K. Jung, H. D. Lim, D. Ahn, S. Lee, and K. Kang, Energy and Environmental Science **8**, 3325 (2015).
[15] X. Li, Y. Wang, D. Wu, L. Liu, S. H. Bo, and G. Ceder, Chemistry of Materials **28**, 6575 (2016).
[16] J. U. Choi, J. Kim, J. Y. Hwang, J. H. Jo, Y. K. Sun, and S. T. Myung, Nano Energy **61**, 284 (2019).
[17] J. S. Zhou, J. A. Alonso, J. T. Han, M. T. Fernández-Díaz, J. G. Cheng, and J. B. Goodenough, Journal of Fluorine Chemistry **132**, 1117 (2011).
[18] S. Margadonna and G. Karotsis, Journal of the American Chemical Society **128**, 16436 (2006).
[19] J. Rodríguez-Carvajal, M. Hennion, F. Moussa, L. Pinsard, and A. Revcolevschi, Physica B: Condensed Matter **234-236**, 848 (1997).
[20] R. Scatena, M. Andrzejewski, R. D. Johnson, and P. Macchi, Journal of Materials Chemistry C **9**, 8051 (2021).
[21] Y. Ren, T. T. Palstra, D. I. Khomskii, E. Pellegrin, A. A. Nugroho, A. A. Menovsky, and G. A. Sawatzky, Nature **396**, 441 (1998).
[22] G. R. Blake, A. A. Nugroho, M. J. Gutmann, and T. T. Palstra, Physical Review B - Condensed Matter and Materials Physics **79**, 045101 (2009).
[23] G. R. Blake, T. T. Palstra, Y. Ren, A. A. Nugroho, and A. A. Menovsky, Physical Review Letters **87**, 245501 (2001).
[24] G. R. Blake, T. T. Palstra, Y. Ren, A. A. Nugroho, and A. A. Menovsky, Physical Review B - Condensed Matter and Materials Physics **65**, 1741121 (2002).
[25] P. Bordet, C. Chaillout, M. Marezio, Q. Huang, A. Santoro, S. W. Cheong, H. Takagi, C. S. Oglesby, and B. Batlogg, Journal of Solid State Chemistry **106**, 253 (1993).
[26] F. Fauth, E. Suard, and V. Caignaert, Physical Review B - Condensed Matter and Materials Physics **65**, 060401 (2002).
[27] T. Nakajima, M. Ichihara, and Y. Ueda, Journal of the Physical Society of Japan **74**, 1572 (2005).
[28] L. D. Dyer, B. S. Borie, and G. P. Smith, Journal of the American Chemical Society **76**, 1499 (1954).
[29] G. S. Phillips, J. M. A. Steele, F. N. Sayed, L. Karger, L. A. V. Nagle-Cocco, A. R. Genreith-Schriever, G. E. Pérez, D. A. Keen, J. Janek, T. Brezesinski, J. D. Bocarsly, S. E. Dutton, and C. P. Grey, Journal of the American Chemical Society **147**, 29042 (2025).
[30] S. Dick, M. Müller, F. Preissinger, and T. Zeiske, Powder Diffraction **12**, 239 (1997).
[31] E. Chappel, M. D. Núñez-Regueiro, G. Chouteau, O. Isnard, and C. Darie, European Physical Journal B **17**, 615 (2000).
[32] M. Sofin and M. Jansen, Zeitschrift fur Naturforschung - Section B Journal of Chemical Sciences **60**, 701 (2005).
[33] L. A. V. Nagle-Cocco, C. L. Bull, C. J. Ridley, and S. E. Dutton, Inorganic Chemistry **61**, 4312 (2022).
[34] L. A. V. Nagle-Cocco, A. R. Genreith-Schriever, J. M. A. Steele, C. Tacconis, J. D. Bocarsly, O. Mathon, J. C. Neuefeind, J. Liu, C. A. O'Keefe, A. L. Goodwin, C. P. Grey, J. S. Evans, and S. E. Dutton, Journal of the American Chemical Society **146**, 29560 (2024).
[35] L. A. V. Nagle-Cocco, J. M. Steele, S. Deng, X. Zhang, D. Daisenberger, A. R. Genreith-Schriever, S. S. Saxena, C. P. Grey, and S. E. Dutton, Journal of Physics Condensed Matter **37**, 205401 (2025).
[36] J. H. Chung, T. Proffen, S. Shamoto, A. M. Ghorayeb, L. Croguennec, W. Tian, B. C. Sales, R. Jin, D. Mandrus, and T. Egami, Physical Review B - Condensed Matter and Materials Physics **71**, 064410 (2005).
[37] Z. Chen, H. Zou, X. Zhu, J. Zou, and J. Cao, Journal of Solid State Chemistry **184**, 1784 (2011).
[38] K. Foyevtsova, I. Elfimov, J. Rottler, and G. A. Sawatzky, Physical Review B **100**, 165104 (2019).
[39] E. Wawrzyńska, R. Coldea, E. M. Wheeler, I. I. Mazin, M. D. Johannes, T. Sörgel, M. Jansen, R. M. Ibberson, and P. G. Radaelli, Physical Review Letters **99**, 157204 (2007).
[40] J.-S. Kang, S. S. Lee, G. Kim, H. J. Lee, H. K. Song, Y. J. Shin, S. W. Han, C. Hwang, M. C. Jung, H. J. Shin, B. H. Kim, S. K. Kwon, and B. I. Min, Physical Review B **76**, 195122 (2007).
[41] J. García-Muñoz, J. Rodríguez-Carvajal, and P. Lacorre, Phys. Rev. B **50**, 978 (1994).
[42] T. Mizokawa, D. I. Khomskii, and G. A. Sawatzky, Phys. Rev. B **61**, 11263 (2000).
[43] J. L. Garcia-Munoz, M. A. G. Aranda, J. A. Alonso, and M. J. Martinez-Lope, Phys. Rev. B **79**, 134432 (2009).
[44] H. Chen, C. L. Freeman, and J. H. Harding, Physical Review B - Condensed Matter and Materials Physics **84**, 085108 (2011).
[45] A. D. Poletayev, R. J. Green, J. E. Swallow, L. An, L. Jones, G. Harris, P. Bencok, R. Sutarto, J. P. Cottom, B. J. Morgan, R. A. House, R. S. Weatherup, and M. S. Islam, Nature Communications **16**, 9379 (2025).
[46] R. J. Green, H. Wadati, T. Z. Regier, A. J. Achkar, C. McMahon, J. P. Clancy, H. A. Dabkowska, B. D. Gaulin, G. A. Sawatzky, and D. G. Hawthorn, arXiv (2020), https://doi.org/10.48550/arXiv.2011.06441.
[47] D. Takegami, K. Kawai, M. Ferreira-Carvalho, S. Rößler, C. E. Liu, C. Y. Kuo, C. F. Chang, A. Minamida, T. Miyazaki, M. Okubo, L. H. Tjeng, and T. Mizokawa, Physical Review Materials **8**, 055401 (2024).
[48] H. Henke, Zeitschrift fur Kristallographie **218**, 617 (2003).
[49] V. Baron, American Mineralogist **83** (1998), 10.2138/am-1998-7-810.
[50] H. Yamaguchi, A. Yamada, and H. Uwe, Physical Review B **58**, 8 (1998).
[51] R. Yokozaki, H. Kobayashi, T. Mandai, and I. Honma, Journal of Alloys and Compounds **872**, 159723 (2021).
[52] P. Patra, I. Naik, H. Bhatt, and S. D. Kaushik, Physica B: Condensed Matter **572**, 199 (2019).
[53] P. F. Schofield, K. S. Knight, S. A. Redfern, and G. Cressey, Acta Crystallographica Section B: Structural Science **53**, 102 (1997).
[54] E. A. Harbourne, H. Barker, Q. Guéroult, J. Cattermull, L. A. V. Nagle-Cocco, N. Roth, J. S. O. Evans, D. A. Keen, and A. L. Goodwin, Chemistry of Materials **36**, 5796 (2024).
[55] J. Cattermull, K. Sada, K. Hurlbutt, S. J. Cassidy, M. Pasta, and A. L. Goodwin, Chemistry of Materials **34**, 5000– (2022).
[56] E. Herdtweck and D. Babel, ZAAC - Journal of Inorganic and General Chemistry **474**, 113 (1981).
[57] C. I. Hiley, C. A. Crawford, C. L. Bull, N. P. Funnell, U. Dey, N. C. Bristowe, R. I. Walton, and M. S. Senn, Physical Review B **112**, 035126 (2025).
[58] A. Nakua, H. Yun, J. N. Reimers, J. E. Greedan, and C. V. Stager, Journal of Solid State Chemistry **91**, 105 (1991).

[59] E. Granado, J. A. Sanjurjo, C. Rettori, J. J. Neumeier, and S. B. Oseroff, Physical Review B - Condensed Matter and Materials Physics **62**, 11304 (2000).

[60] T. Chatterji, F. Fauth, B. Ouladdiaf, P. Mandal, and B. Ghosh, Physical Review B - Condensed Matter and Materials Physics **68**, 052406 (2003).

[61] J.-S. Zhou and J. B. Goodenough, Physical Review B **68**, 144406 (2003).

[62] X. Qiu, T. Proffen, J. F. Mitchell, and S. J. Billinge, Physical Review Letters **94**, 177203 (2005).

[63] M. V. Kharlamova and A. Arulraj, JETP Letters **89**, 301 (2009).

[64] T. Chatterji, B. Ouladdiaf, P. Mandal, and B. Ghosh, Solid State Communications **131**, 75 (2004).

[65] R. A. Souza, N. M. Souza-Neto, A. Y. Ramos, H. C. Tolentino, and E. Granado, Physical Review B - Condensed Matter and Materials Physics **70**, 214426 (2004).

[66] P. Mondal, D. Bhattacharya, and P. Mandal, Physical Review B - Condensed Matter and Materials Physics **84**, 075111 (2011).

[67] F. E. Ramirez, B. B. Cunha, W. A. Alves, R. F. Jardim, R. Muccillo, and J. A. Souza, Phase Transitions **84**, 284 (2011).

[68] P. M. Thygesen, C. A. Young, E. O. Beake, F. D. Romero, L. D. Connor, T. E. Proffen, A. E. Phillips, M. G. Tucker, M. A. Hayward, D. A. Keen, and A. L. Goodwin, Physical Review B **95**, 174107 (2017).

[69] T. H. Tran, T. C. Bach, N. H. Pham, Q. H. Nguyen, C. D. Sai, H. N. Nguyen, V. T. Nguyen, T. T. Nguyen, K. H. Ho, and Q. K. Doan, Materials Science in Semiconductor Processing **89**, 121 (2019).

[70] M. Saint-Paul and P. Lejay, Physica B: Condensed Matter **352**, 353 (2004).

[71] B. R. M. Tragheim, E. A. Harbourne, C. Ritter, A. L. Goodwin, and M. S. Senn, Physical Review B **112**, 115119 (2025).

[72] B. Batnaran, A. L. Goodwin, M. A. Hayward, and V. L. Deringer, arXiv (2025), https://doi.org/10.48550/arXiv.2510.25414.

[73] S. Yano, D. Louca, J. C. Neuefeind, J. Q. Yan, J. S. Zhou, and J. B. Goodenough, Physical Review B - Condensed Matter and Materials Physics **90**, 214111 (2014).

[74] S. Margadonna and G. Karotsis, Journal of Materials Chemistry **17**, 2013 (2007).

[75] L. G. Marshall, J. Zhou, J. Zhang, J. Han, S. C. Vogel, X. Yu, Y. Zhao, M. T. Fernández-Díaz, J. Cheng, and J. B. Goodenough, Physical Review B - Condensed Matter and Materials Physics **87**, 014109 (2013).

[76] M. Heinrich, H. A. Krug von Nidda, A. Krimmel, A. Loidl, R. M. Eremina, A. D. Ineev, B. I. Kochelaev, A. V. Prokofiev, and W. Assmus, Physical Review B - Condensed Matter and Materials Physics **67**, 224418 (2003).

[77] S. Sicolo, M. Mock, M. Bianchini, and K. Albe, Chemistry of Materials **32**, 10096 (2020).

[78] M. R. Ahmed and G. A. Gehring, Journal of Physics A: Mathematical and General **38**, 4047 (2005).

[79] M. R. Ahmed and G. A. Gehring, Physical Review B - Condensed Matter and Materials Physics **74**, 014420 (2006).

[80] M. R. Ahmed and G. A. Gehring, Physical Review B - Condensed Matter and Materials Physics **79**, 174106 (2009).

[81] P. Vassilaras, X. Ma, X. Li, and G. Ceder, Journal of The Electrochemical Society **160**, A207 (2013).

[82] J. M. A. Steele, A. R. Genreith-Schriever, J. D. Bocarsly, L. A. V. Nagle-Cocco, F. N. Sayed, M. Juramy, C. A. O'Keefe, F. Orlandi, P. Manuel, E. Dutton, and C. P. Grey, Chemistry of Materials **37**, 2581 (2025).

[83] M. Bianchini, M. Roca-Ayats, P. Hartmann, T. Brezesinski, and J. Janek, Angewandte Chemie - International Edition **58**, 10434 (2019).

[84] A. R. Genreith-Schriever, H. Banerjee, A. S. Menon, E. N. Bassey, L. F. J. Piper, C. P. Grey, and A. J. Morris, Joule **7**, 1623 (2023).

[85] M. D. Radin, J. C. Thomas, and A. Van Der Ven, Physical Review Materials **4**, 043601 (2020).

[86] A. R. Genreith-Schriever, A. Alexiu, G. S. Phillips, C. S. Coates, L. A. V. Nagle-Cocco, J. D. Bocarsly, F. N. Sayed, S. E. Dutton, and C. P. Grey, Chemistry of Materials **36**, 2289 (2024).

[87] Q. Jacquet, K. Kummer, M. Guignard, E. Grépin, S. Mariyappan, N. B. Brookes, and S. Lyonnard, The Journal of Physical Chemistry C , 17437 (2025).

[88] N. Metropolis, A. W. Rosenbluth, M. N. Rosenbluth, A. H. Teller, and E. Teller, The Journal of Chemical Physics **21**, 1087 (1953).

[89] G. Van Rossum, *Python tutorial*, Tech. Rep. (Stichting Mathematisch Centrum, Amsterdam, 1995).

[90] OpenAI, J. Achiam, S. Adler, S. Agarwal, L. Ahmad, I. Akkaya, F. L. Aleman, D. Almeida, J. Altenschmidt, S. Altman, S. Anadkat, R. Avila, I. Babuschkin, S. Balaji, V. Balcom, P. Baltescu, H. Bao, M. Bavarian, J. Belgum, I. Bello, J. Berdine, G. Bernadett-Shapiro, C. Berner, L. Bogdonoff, O. Boiko, M. Boyd, A.-L. Brakman, G. Brockman, T. Brooks, M. Brundage, K. Button, T. Cai, R. Campbell, A. Cann, B. Carey, C. Carlson, R. Carmichael, B. Chan, C. Chang, F. Chantzis, D. Chen, S. Chen, R. Chen, J. Chen, M. Chen, B. Chess, C. Cho, C. Chu, H. W. Chung, D. Cummings, J. Currier, Y. Dai, C. Decareaux, T. Degry, N. Deutsch, D. Deville, A. Dhar, D. Dohan, S. Dowling, S. Dunning, A. Ecoffet, A. Eleti, T. Eloundou, D. Farhi, L. Fedus, N. Felix, S. P. Fishman, J. Forte, I. Fulford, L. Gao, E. Georges, C. Gibson, V. Goel, T. Gogineni, G. Goh, R. Gontijo-Lopes, J. Gordon, M. Grafstein, S. Gray, R. Greene, J. Gross, S. S. Gu, Y. Guo, C. Hallacy, J. Han, J. Harris, Y. He, M. Heaton, J. Heidecke, C. Hesse, A. Hickey, W. Hickey, P. Hoeschele, B. Houghton, K. Hsu, S. Hu, X. Hu, J. Huizinga, S. Jain, S. Jain, J. Jang, A. Jiang, R. Jiang, H. Jin, D. Jin, S. Jomoto, B. Jonn, H. Jun, T. Kaftan, . Kaiser, A. Kamali, I. Kanitscheider, N. S. Keskar, T. Khan, L. Kilpatrick, J. W. Kim, C. Kim, Y. Kim, J. H. Kirchner, J. Kiros, M. Knight, D. Kokotajlo, . Kondraciuk, A. Kondrich, A. Konstantinidis, K. Kosic, G. Krueger, V. Kuo, M. Lampe, I. Lan, T. Lee, J. Leike, J. Leung, D. Levy, C. M. Li, R. Lim, M. Lin, S. Lin, M. Litwin, T. Lopez, R. Lowe, P. Lue, A. Makanju, K. Malfacini, S. Manning, T. Markov, Y. Markovski, B. Martin, K. Mayer, A. Mayne, B. McGrew, S. M. McKinney, C. McLeavey, P. McMillan, J. McNeil, D. Medina, A. Mehta, J. Menick, L. Metz, A. Mishchenko, P. Mishkin, V. Monaco, E. Morikawa, D. Mossing, T. Mu, M. Murati, O. Murk, D. Mély, A. Nair, R. Nakano, R. Nayak, A. Neelakantan, R. Ngo, H. Noh, L. Ouyang, C. O'Keefe, J. Pachocki, A. Paino, J. Palermo, A. Pantuliano, G. Parascandolo, J. Parish, E. Parparita, A. Passos, M. Pavlov, A. Peng, A. Perelman, F. d. A. B. Peres, M. Petrov, H. P. d. O. Pinto, Michael, Pokorny, M. Pokrass, V. H. Pong, T. Powell, A. Power, B. Power, E. Proehl, R. Puri, A. Radford, J. Rae, A. Ramesh, C. Raymond, F. Real, K. Rimbach, C. Ross, B. Rotsted,

H. Roussez, N. Ryder, M. Saltarelli, T. Sanders, S. Santurkar, G. Sastry, H. Schmidt, D. Schnurr, J. Schulman, D. Selsam, K. Sheppard, T. Sherbakov, J. Shieh, S. Shoker, P. Shyam, S. Sidor, E. Sigler, M. Simens, J. Sitkin, K. Slama, I. Sohl, B. Sokolowsky, Y. Song, N. Staudacher, F. P. Such, N. Summers, I. Sutskever, J. Tang, N. Tezak, M. B. Thompson, P. Tillet, A. Tootoonchian, E. Tseng, P. Tuggle, N. Turley, J. Tworek, J. F. C. Uribe, A. Vallone, A. Vijayvergiya, C. Voss, C. Wainwright, J. J. Wang, A. Wang, B. Wang, J. Ward, J. Wei, C. Weinmann, A. Welihinda, P. Welinder, J. Weng, L. Weng, M. Wiethoff, D. Willner, C. Winter, S. Wolrich, H. Wong, L. Workman, S. Wu, J. Wu, M. Wu, K. Xiao, T. Xu, S. Yoo, K. Yu, Q. Yuan, W. Zaremba, R. Zellers, C. Zhang, M. Zhang, S. Zhao, T. Zheng, J. Zhuang, W. Zhuk, and B. Zoph, arXiv (2024), doi.org/10.48550/arXiv.2303.08774.

[91] J. D. Hunter, Computing in Science and Engineering **9** (2007), 10.1109/MCSE.2007.55.

[92] K. Momma and F. Izumi, Journal of Applied Crystallography **44**, 1272 (2011).

SUPPLEMENTARY INFORMATION

LIST OF TABLES

S1 Unique phases in the (J_1,J_2) phase diagram for perovskites 18

LIST OF FIGURES

S1 G-type orbital order as reported in literature 14
S2 Collinear orbital order in perovskites as reported in literature 15
S3 Various proposed layered nickelate orbital order as reported in literature 16
S4 Collinear orbital order in spinels from literature 17
S5 Summary of Monte Carlo perovskite run with static ρ to reproduce phase 1 of (J_1, J_2) phase diagram . 19
S6 Summary of Monte Carlo perovskite run with static ρ to reproduce phase 2 of (J_1, J_2) phase diagram . 20
S7 Summary of Monte Carlo perovskite run with static ρ to reproduce phase 3 of (J_1, J_2) phase diagram . 21
S8 Summary of Monte Carlo perovskite run with static ρ to reproduce phase 4 of (J_1, J_2) phase diagram . 22
S9 Summary of Monte Carlo perovskite run with static ρ to reproduce phase 5 of (J_1, J_2) phase diagram . 23
S10 Summary of Monte Carlo perovskite run with static ρ to reproduce phase 6 of (J_1, J_2) phase diagram . 24
S11 Summary of Monte Carlo perovskite run with dynamic ρ to reproduce phase 1 of (J_1, J_2) phase diagram 25
S12 Summary of Monte Carlo perovskite run with dynamic ρ to reproduce phase 5 of (J_1, J_2) phase diagram 26
S13 Dependence of heat capacity and energy on temperature for the two perovskite orderings tested, plotted on a non-logarithmic x-axis 27
S14 Dependence of heat capacity and energy on temperature 2D layered nickelate lattice, plotted on a non-logarithmic x-axis 28
S15 Comparison of $\langle\rho\rangle$ with temperature for the various cases considered on perovskite and 2D nickelate lattices 29
S16 Temperature-dependence of energy, $\langle\rho\rangle$, and C for a $4 \times 4 \times 4$ perovskite supercell 31
S17 Temperature-dependence of energy, $\langle\rho\rangle$, and C for a $6 \times 6 \times 6$ perovskite supercell 32
S18 Final histogram of ρ distribution for layered nickelate with $K_{\text{oxy}} = 1$ 33
S19 Final histogram of ρ distribution for layered nickelate with $K_{\text{oxy}} = 1$ 34
S20 Final histogram of ρ distribution for layered nickelate with $K_{\text{oxy}} \to \infty$ 35
S21 Final histogram of ρ distribution for phase 1 (collinear) perovskite 36
S22 Final histogram of ρ distribution for phase 5 (C-type) perovskite 37

S1. Other reported orderings from literature

Figure S1 shows the transition between G-type and C-type orbital order reported[23,24] for YVO_3. C-type orbital order is studied in this present work; G-type orbital order is not obtained in the phase diagram of Ahmed and Gehring and would likely require an extended model including additional J terms. Both orbital orderings shown here are not strictly Jahn–Teller distortions (although d^2 vanadates do contain electronic degeneracy).

Figure S2 shows the two reported orbital orderings of $La_{0.5}Ba_{0.5}CoO_6$ perovskite[26,27], which differ depending on whether the A site is ordered or disordered. Both are collinear ordering, but JT distortions are compressive and elongational respectively. It should be noted that the compressive structure[27] exhibits some Q_2 component which is not a degree of freedom in our simulations.

Figure S3 shows various proposed orbital orderings for $LiNiO_2$, including the collinear structure which we find as being the ideal structure within domains, and the trimers and dimers which we observe at the interfaces of orbitally-ordered domains.

Orbital ordering in spinels is almost invariably found to be collinear. Figure S4 shows a depiction of the octahedral elongations in this ordering.

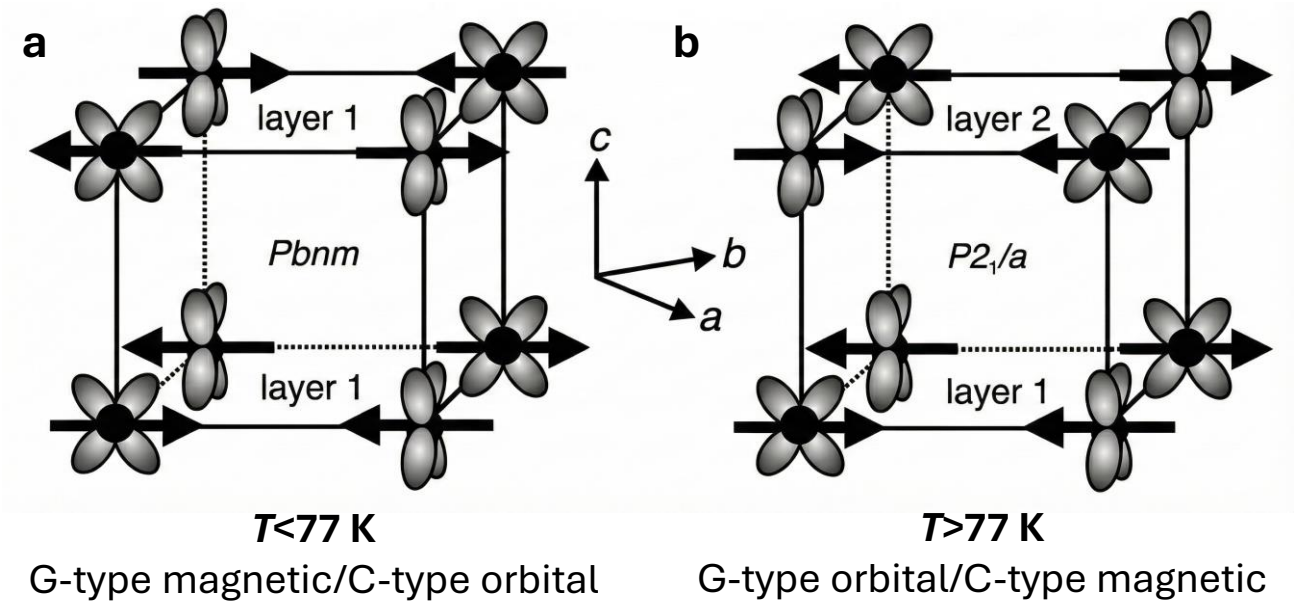

FIG. S1: The orbital ordering in the perovskite YVO_3 at low (left) and high (right) temperatures, representing C- and G-type orbital order respectively, as reported by Blake *et al.*[24] The C-type orbital order (left) matches that of $LaMnO_3$, corresponding to phase 5 of the phase diagram of Ahmed and Gehring[79]. The G-type orbital order cannot be recovered from the phase diagram of Ahmed and Gehring.

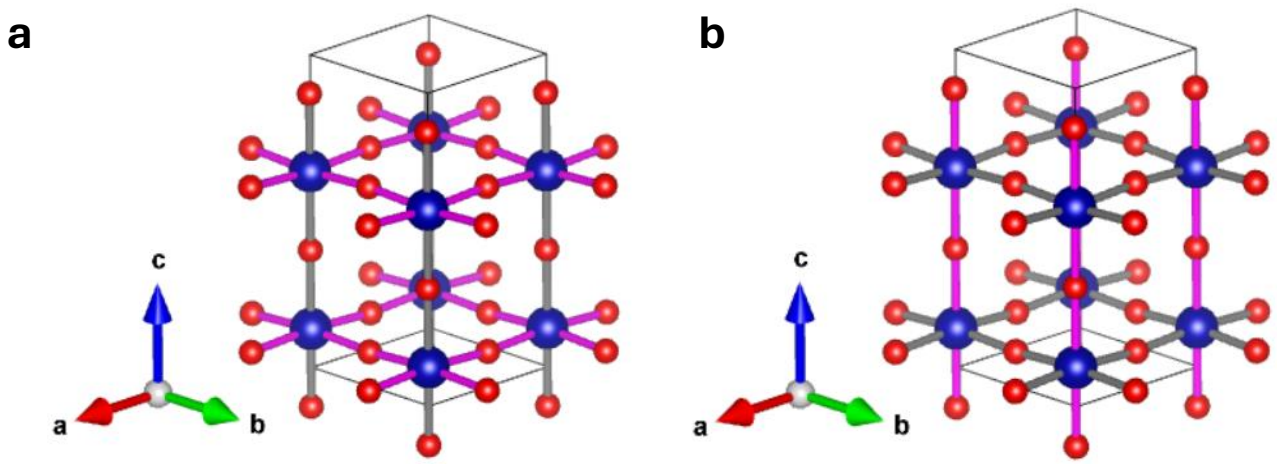

FIG. S2: The orbital ordering in the perovskite $La_{0.5}Ba_{0.5}CoO_3$, as reported for (a) ordered[27] and (b) disordered[26] A-site cations. Here, A-site cations are excluded, blue cations are Co, grey bonds are short and pink bonds are long.

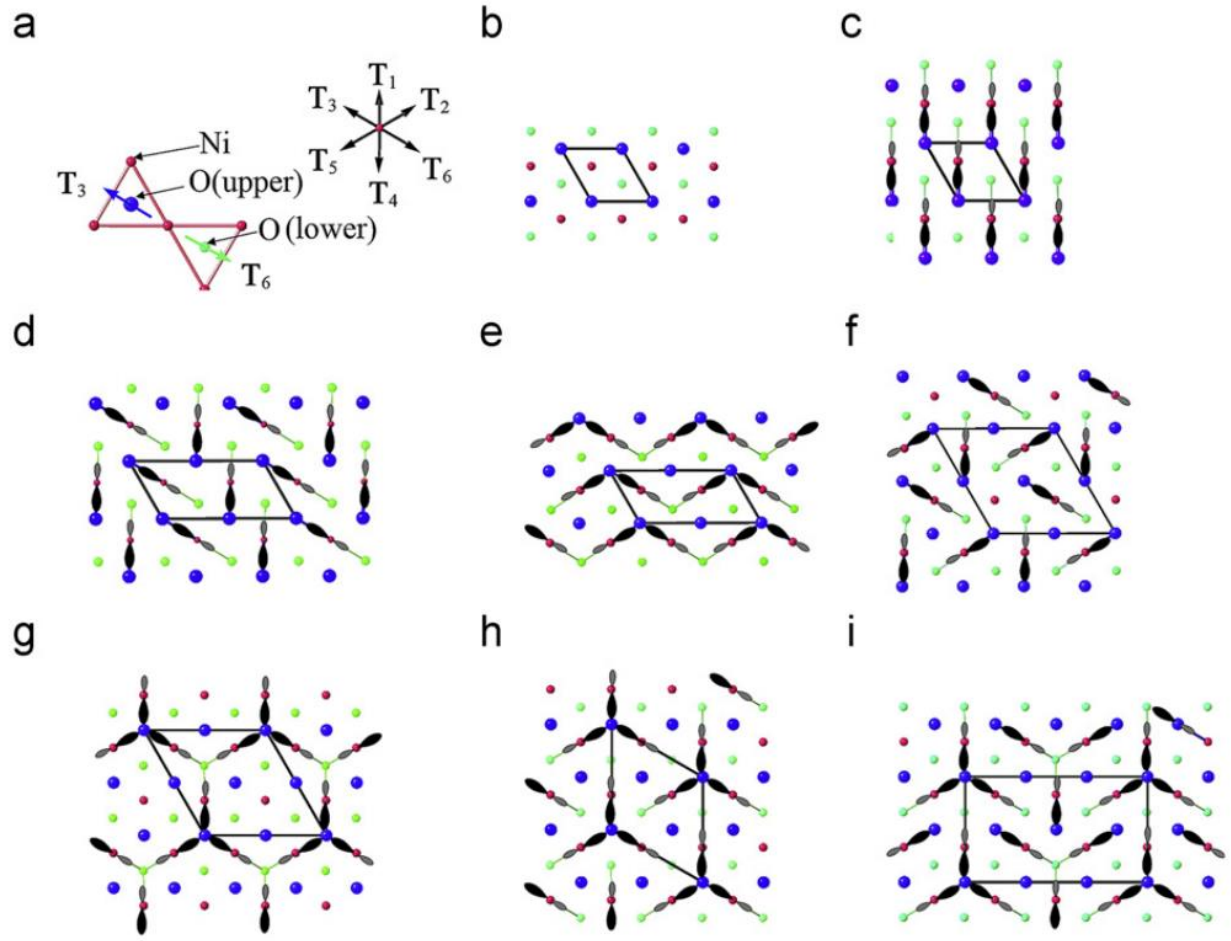

FIG. S3: Various proposed models for layered nickelate orbital ordering. Models viewed along the c axis. The red balls denote Ni ions, the blue and green balls are oxygen ions in the upper plane and in the lower plane, respectively. Only the shifted oxygen ions are linked with the Ni ions in the sketches. The unit cell of each model is outlined with black lines. (a) Definitions of the six shift directions in the flat oxygen plane: $T_1 = a + 2b$; $T_2 = 2a + b$; $T_3 = -a + b$; $T_4 = -a - 2b$; $T_5 = -2a - b$; $T_6 = a - b$. Vectors a, b and c are the basis vectors of the $R\bar{3}m$ hexagonal lattice. (b) $R\bar{3}m$. (c) $C2/m$. (d) Zigzag. (e) Dimer. (f) Windmill. (g) Honeycomb. (h) Trimer. (i) Alternating trimer. Reprinted from Journal of Solid State Chemistry, Vol. 184, Issue 7, Chen, Zhenlian; Zou, Huamin; Zhu, Xiaopeng; Zou, Jie; Cao, Jiefeng. *First-principle investigation of Jahn–Teller distortion and topological analysis of chemical bonds in* $LiNiO_2$, pp. 1784–1790, Copyright (2011), with permission from Elsevier.[37].

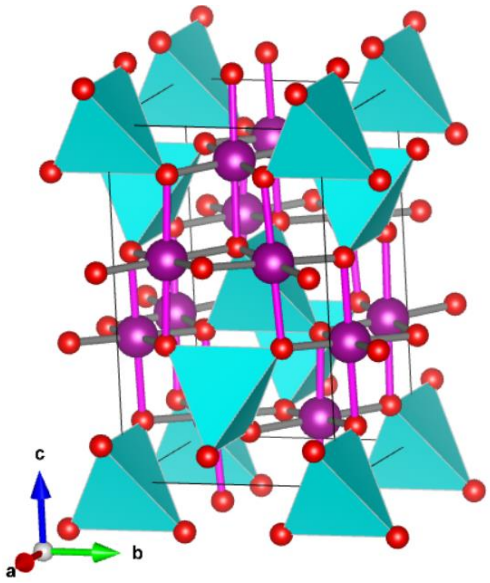

FIG. S4: Proposed collinear orbital ordering in spinels with $ZnMn_2O_4$ taken as an example. Pink bonds indicate the axes of elongation of octahedra.

S2. Reproducing the anisotropic Potts model perovskite phase diagram with static ρ

To validate our code, we tested our code using the specific conditions matching that of Ahmed and Gehring's Monte Carlo simulations[78,79]. In this case, ρ is fixed to 1 for all JT-active sites, and $p_{\text{switch}} = 0$ to ensure there is no variation in the JT activity of each site. This is a specific case of the Hamiltonian in Equation 1 where $\alpha = \beta = 0$. Table S1 lists the phases in the anisotropic Potts phase diagram which were identified by Ahmed and Gehring[78], along with the conditions by which we reproduced this phase. Figures S5 to S10 shows the results of Monte Carlo runs under these conditions to reproduce the six phases. We find that overall the phases are reproduced, but often we had to use several runs with varying T_{max} to reproduce the expected ordering.

Phase	**Constraints in** (J_1, J_2)	Values tested	Static ρ test		Dynamic ρ test
			T_{max}	Figure	
1	$J_2 < 0,\ \ J_1 < -J_2$	$J_2 = J_1 = -1$	100	Figure S5	Figure S11
2	$J_2 > 0,\ \ J_1 < -2J_2$	$J_1 = -1,\ J_2 = 0.1$	15	Figure S6	-
3	$J_2 > 0,\ \ 0 > J_1 > -2J_2$	$J_1 = -1,\ J_2 = 1$	15	Figure S7	-
4	$J_2 > 0,\ \ J_1 > 0$	$J_1 = J_2 = 1$	15	Figure S8	-
5	$J_2 < 0,\ \ J_1 > -2J_2$	$J_1 = 1,\ J_2 = -0.1$	15	Figure S9	Figures 3 and S12
6	$J_2 < 0,\ \ -2J_2 > J_1 > -J_2$	$J_1 = 1,\ J_2 = -0.75$	100	Figure S10	-

TABLE S1: Phases of the anisotropic Potts model reported by Ahmed and Gehring[78,79]. This is a specific case of the Hamiltonian in Equation 1 where $\alpha = \beta = 0$, and in the simulations $p_{\text{switch}} = 0$. Simulated annealing was used with variable T_{max}, as described in Equation A1, before settling on a final $T = 0.001$. Note that we use opposite sign conventions for J_1 and J_2 compared with Ahmed and Gehring. Each run lasted for 5×10^6 iterations.

Beyond this, we then tested a dynamic ρ model, in which $\alpha \neq 0$ and $\beta \neq 0$, and $p_{\text{switch}} = 0.5$, to ensure our extended Hamiltonian in Equation 1 can also reproduce the phase diagram. We test this on phases 1 and 5, shown in Figures S11 and 3 respectively.

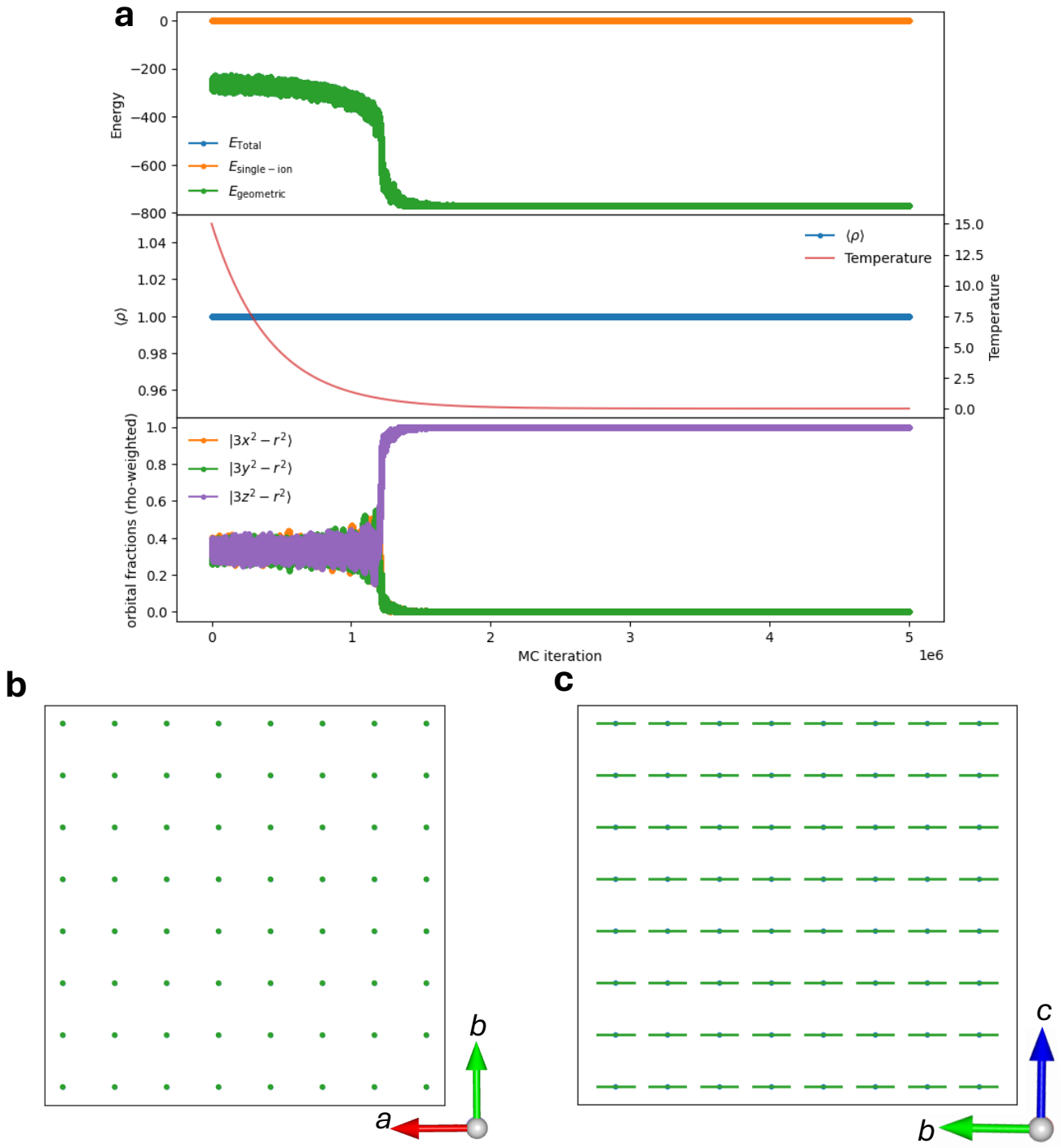

FIG. S5: The results of a Monte Carlo refinement with static $\rho = 1$ ($p_{\text{switch}} = 0$), reproducing Phase 1 of the Ahmed and Gehring[78] phase diagram for the anisotropic Potts model in a perovskite. (a) Energy with iteration (top), mean ρ and temperature against iteration (middle), fractional occupations of e_g orbitals in each direction (bottom). (b) Example configuration in the ab-plane in a randomly-selected cross-section. (c) Example configuration in the bc-plane in a randomly-selected cross-section. Energy parameters $\alpha = \beta = 0$ from equation 1. Simulated annealing was used before settling on a final $T = 0.001$. This run lasted for 5×10^6 iterations.

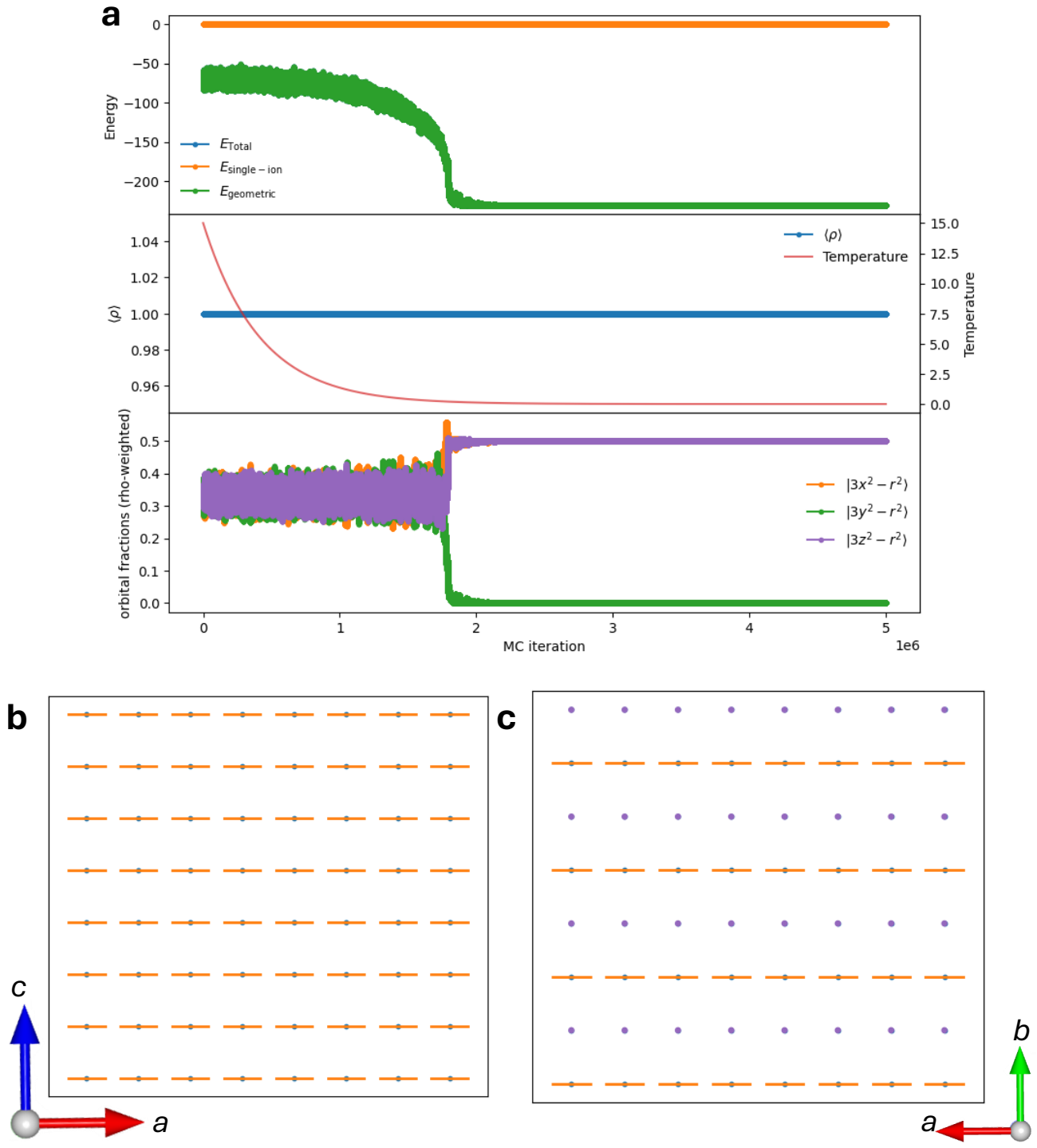

FIG. S6: The results of a Monte Carlo refinement with static $\rho = 1$ ($p_{\text{switch}} = 0$), reproducing Phase 2 of the Ahmed and Gehring[78] phase diagram for the anisotropic Potts model in a perovskite. (a) Energy with iteration (top), mean ρ and temperature against iteration (middle), fractional occupations of e_g orbitals in each direction (bottom). (b) Example configuration in the ac-plane in a randomly-selected cross-section. (c) Example configuration in the ab-plane in a randomly-selected cross-section. Energy parameters $\alpha = \beta = 0$ from equation 1. Simulated annealing was used before settling on a final $T = 0.001$. This run lasted for 5×10^6 iterations.

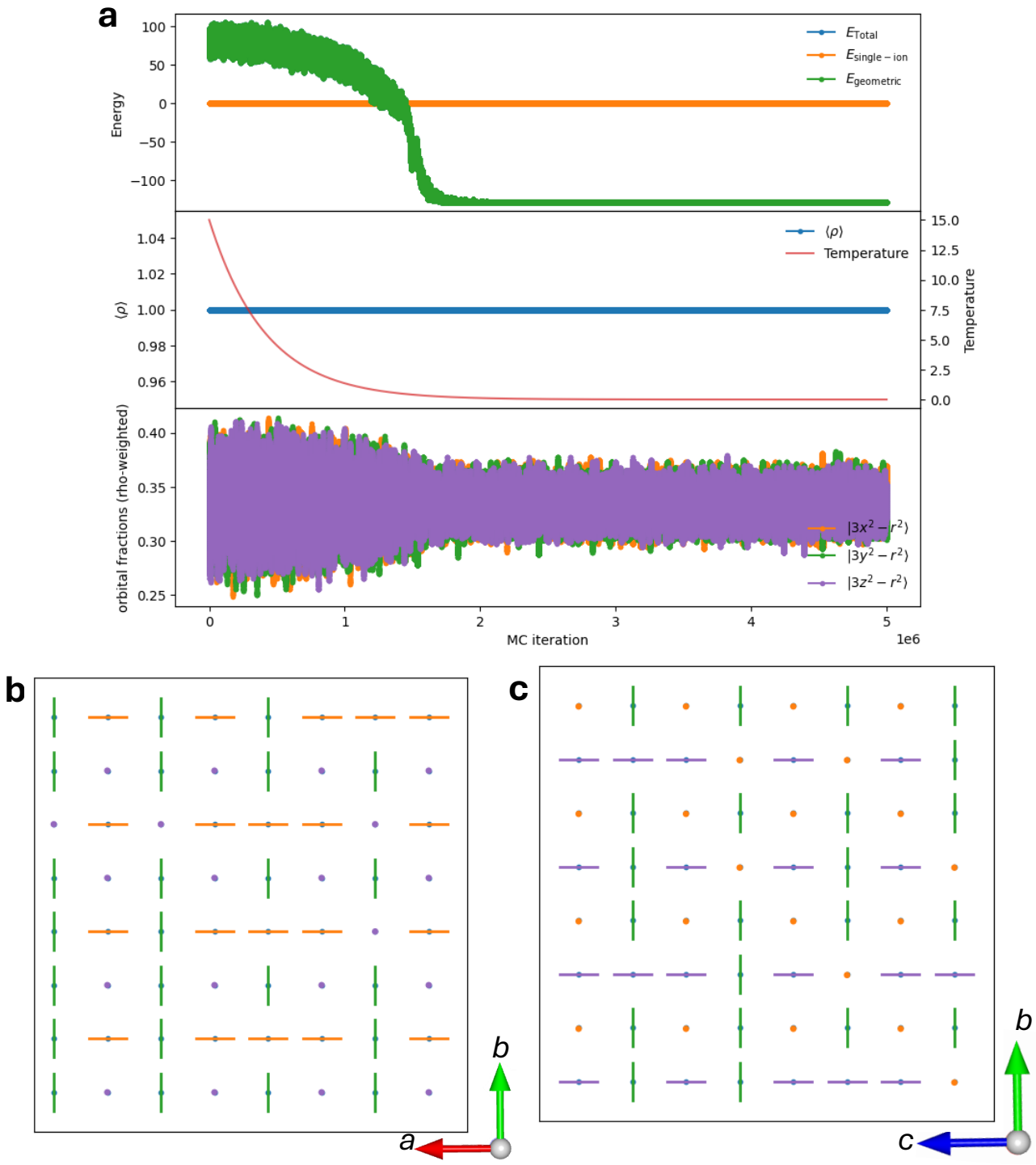

FIG. S7: The results of a Monte Carlo refinement with static $\rho = 1$ ($p_{\text{switch}} = 0$), reproducing Phase 3 of the Ahmed and Gehring[78] phase diagram for the anisotropic Potts model in a perovskite. (a) Energy with iteration (top), mean ρ and temperature against iteration (middle), fractional occupations of e_g orbitals in each direction (bottom). (b) Example configuration in the ab-plane in a randomly-selected cross-section. (c) Example configuration in the bc-plane in a randomly-selected cross-section. Energy parameters $\alpha = \beta = 0$ from equation 1. Simulated annealing was used before settling on a final $T = 0.001$. This run lasted for 5×10^6 iterations. While there are clearly defects in the structure relative to the phase 3 "cage" ground state, the proposed "cage"-ordering is broadly maintained.

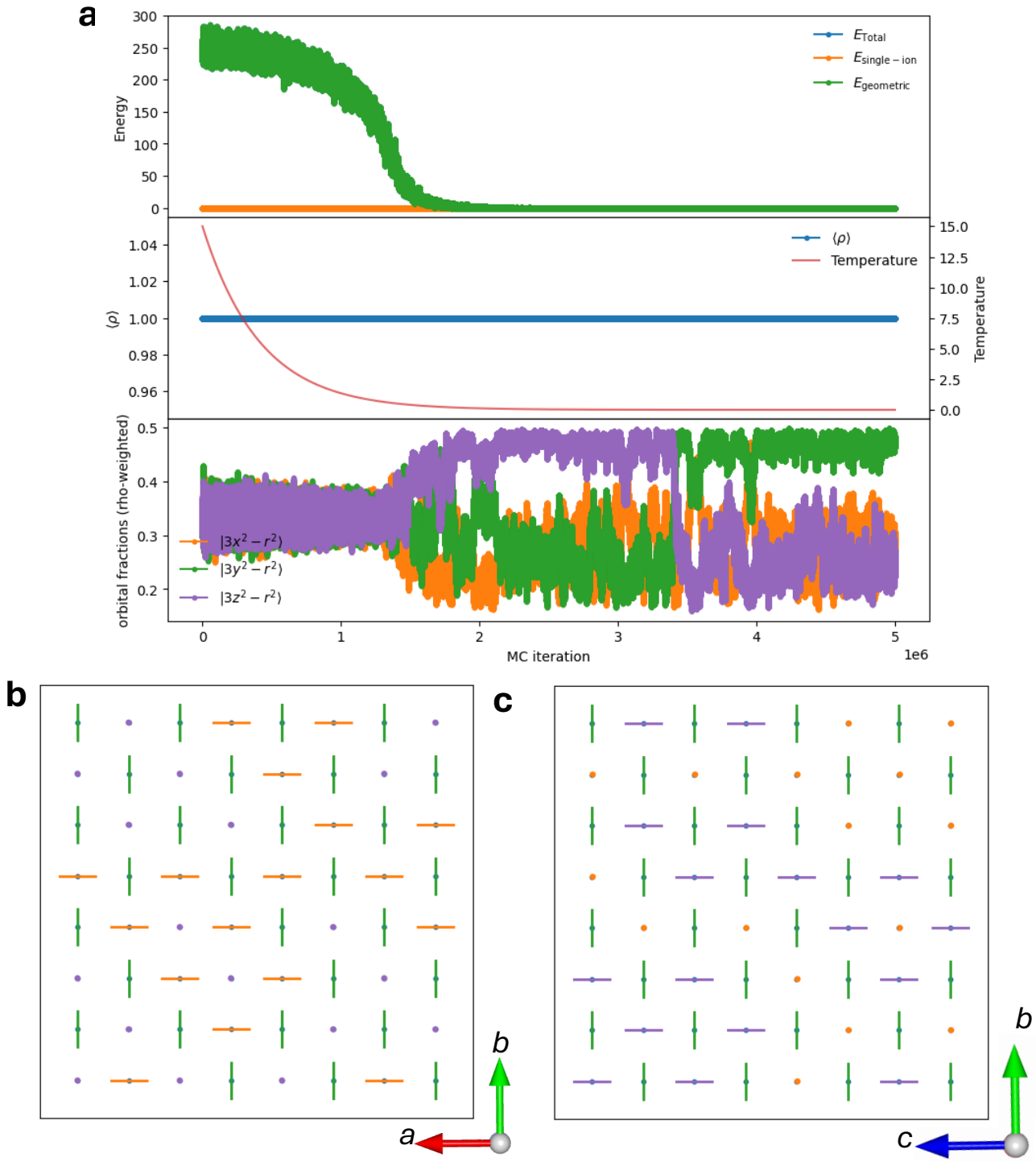

FIG. S8: The results of a Monte Carlo refinement with static $\rho = 1$ ($p_{\text{switch}} = 0$), reproducing the antiferromagnetic Phase 4 of the Ahmed and Gehring[78] phase diagram for the anisotropic Potts model in a perovskite. (a) Energy with iteration (top), mean ρ and temperature against iteration (middle), fractional occupations of e_g orbitals in each direction (bottom). (b) Example configuration in the ab-plane in a randomly-selected cross-section. (c) Example configuration in the bc-plane in a randomly-selected cross-section. Energy parameters $\alpha = \beta = 0$ from equation 1. Simulated annealing was used before settling on a final $T = 0.001$. This run lasted for 5×10^6 iterations. The switching behaviour we see even at lowest temperature suggests instability associated with having antiferromagnetic $J_1 = J_2$, although the antiferromagnetic behaviour reported by Ahmed and Gehring is essentially reproduced.

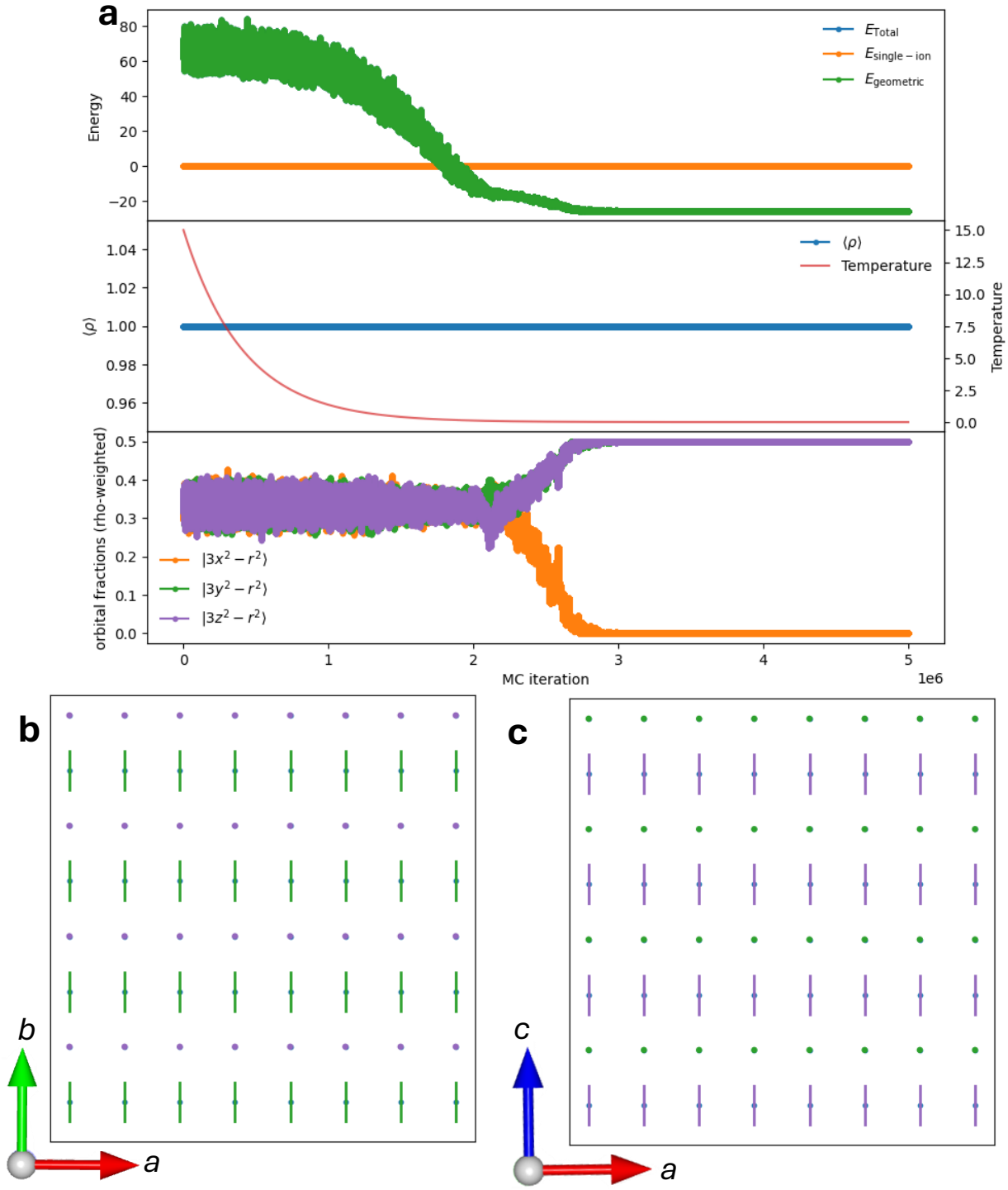

FIG. S9: The results of a Monte Carlo refinement with static $\rho = 1$ ($p_{\text{switch}} = 0$), reproducing Phase 5 of the Ahmed and Gehring[78] phase diagram for the anisotropic Potts model in a perovskite. (a) Energy with iteration (top), mean ρ and temperature against iteration (middle), fractional occupations of e_g orbitals in each direction (bottom). (b) Example configuration in the *ab*-plane in a randomly-selected cross-section. (c) Example configuration in the *ac*-plane in a randomly-selected cross-section. Energy parameters $\alpha = \beta = 0$ from equation 1. Simulated annealing was used before settling on a final $T = 0.001$. This run lasted for 5×10^6 iterations. We note the presence of a defect here. As seen in the *ab*-plane, there is a single collinear plane which has the effect that ∼12.5% of sites have an elongation in $|3y^2 - r^2>$, even though the energy is mimimised analytically *via* the ordering in the other 7 (of 8) planes. With slower annealing we could likely remove this defect, but it is instructive to keep it in place to show the tendency of Monte Carlo simulations towards local minima at low temperatures, even with simulated annealing.

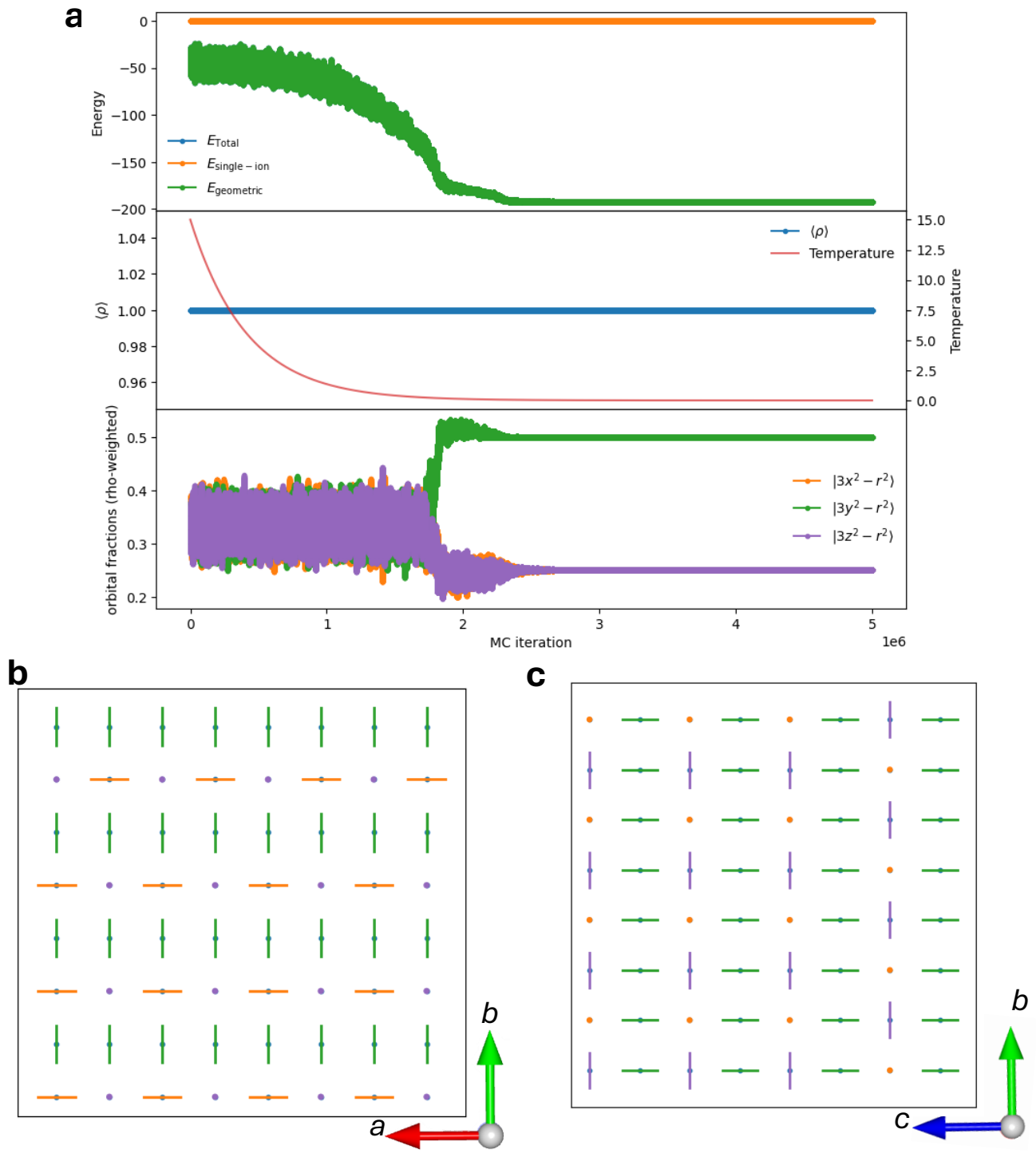

FIG. S10: The results of a Monte Carlo refinement with static $\rho = 1$ ($p_{\text{switch}} = 0$), reproducing Phase 6 of the Ahmed and Gehring[78] phase diagram for the anisotropic Potts model in a perovskite. (a) Energy with iteration (top), mean ρ and temperature against iteration (middle), fractional occupations of e_g orbitals in each direction (bottom). (b) Example configuration in the ab-plane in a randomly-selected cross-section. (c) Example configuration in the bc-plane in a randomly-selected cross-section. Energy parameters $\alpha = \beta = 0$ from equation 1. Simulated annealing was used before settling on a final $T = 0.001$. This run lasted for 5×10^6 iterations.

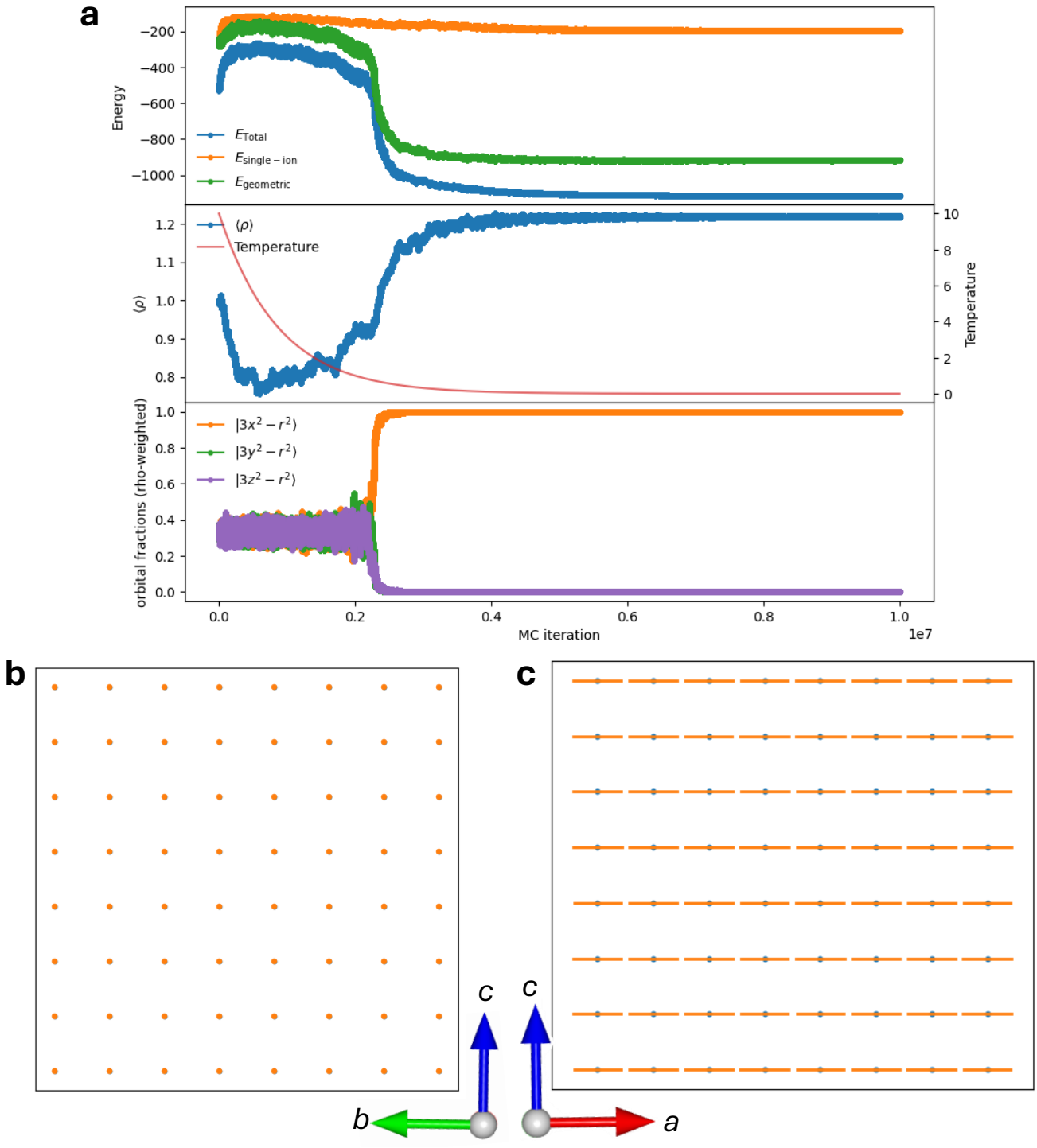

FIG. S11: The results of a Monte Carlo refinement with dynamic ρ ($p_{\text{switch}} = 1/2$), reproducing Phase 1 of the Ahmed and Gehring[78] phase diagram for the anisotropic Potts model in a perovskite. (a) Energy with iteration (top), mean ρ and temperature against iteration (middle), fractional occupations of e_g orbitals in each direction (bottom). (b) Example configuration in the bc-plane in a randomly-selected cross-section. (c) Example configuration in the ac-plane in a randomly-selected cross-section. Energy parameters $\alpha = -1$,$\beta = -1$ from equation 1. Simulated annealing was used before settling on a final $T = 0.001$. This run lasted for 10^7 iterations.

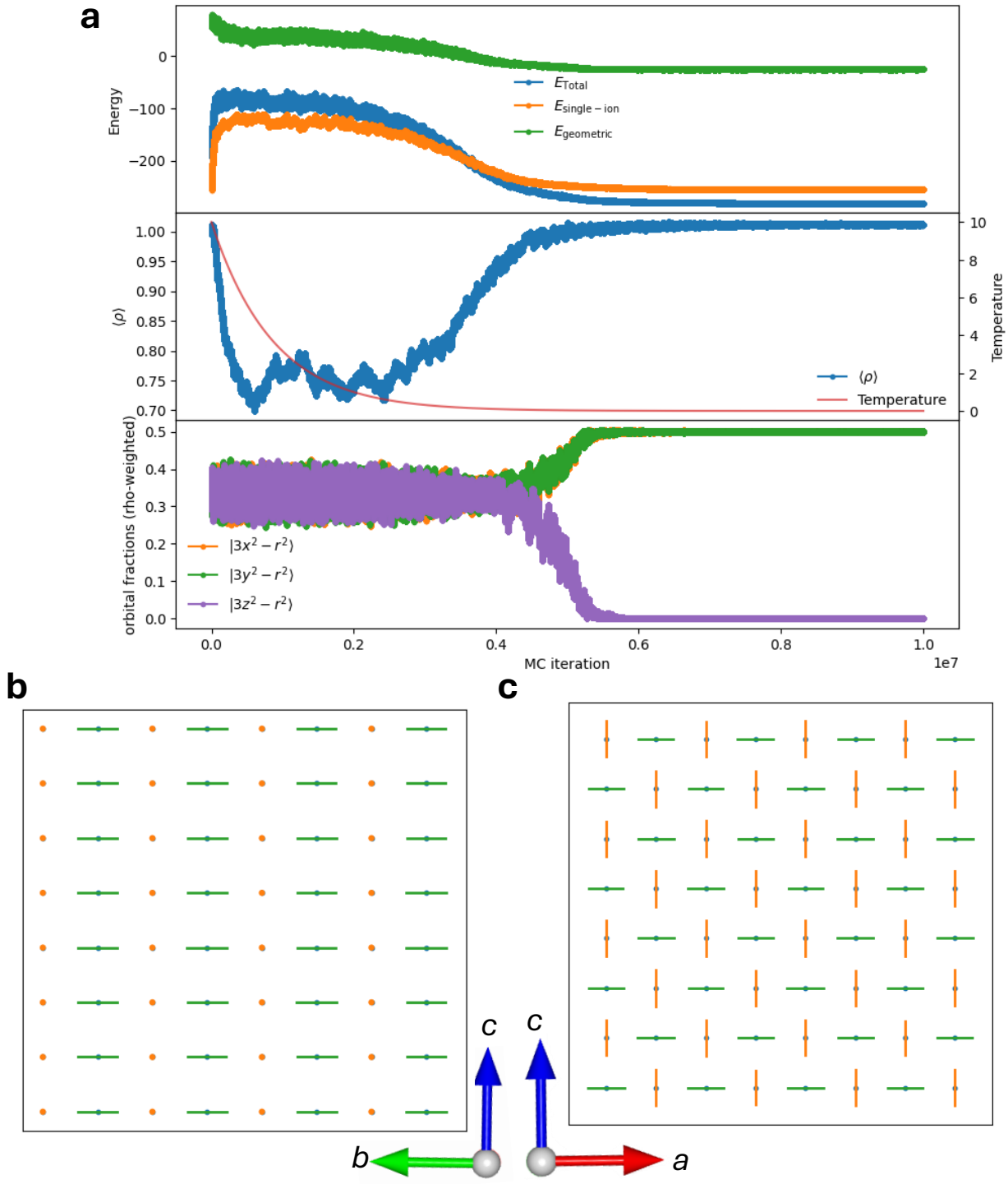

FIG. S12: The results of a Monte Carlo refinement with dynamic ρ ($p_{\text{switch}} = 1/2$), reproducing Phase 5 of the Ahmed and Gehring[78] phase diagram for the anisotropic Potts model in a perovskite. (a) Energy with iteration (top), mean ρ and temperature against iteration (middle), fractional occupations of e_g orbitals in each direction (bottom). (b) Example configuration in the bc-plane in a randomly-selected cross-section. (c) Example configuration in the ac-plane in a randomly-selected cross-section. Energy parameters $\alpha = -1, \beta = 1/2$ from equation 1. Simulated annealing was used before settling on a final $T = 0.001$. This run lasted for 10^7 iterations.

S3. Non-logarithmic plots of energy with temperature

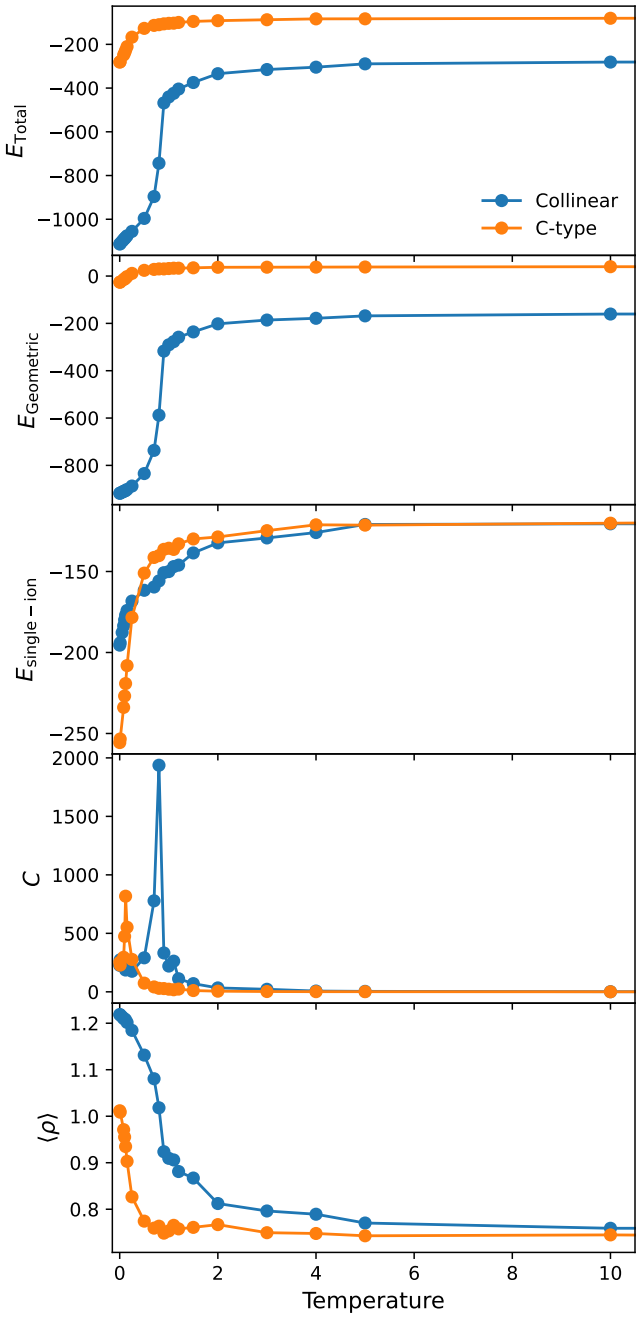

FIG. S13: The mean energy terms E_{total}, $E_{\text{Geometric}}$ (Eq 3), and $E_{\text{single-ion}}$ (Eq 2), heat capacity C, and $\langle\rho\rangle$, averaged over the final 10% of iterations in Monte Carlo simulations, as a function of temperature for the collinear and C-type orbital orderings in a $8 \times 8 \times 8$ perovskite lattice. The Monte Carlo simulations ran for 10^7 iterations in total at each temperature. This figure is reproduced on a logarithmic temperature scale in Figure 4.

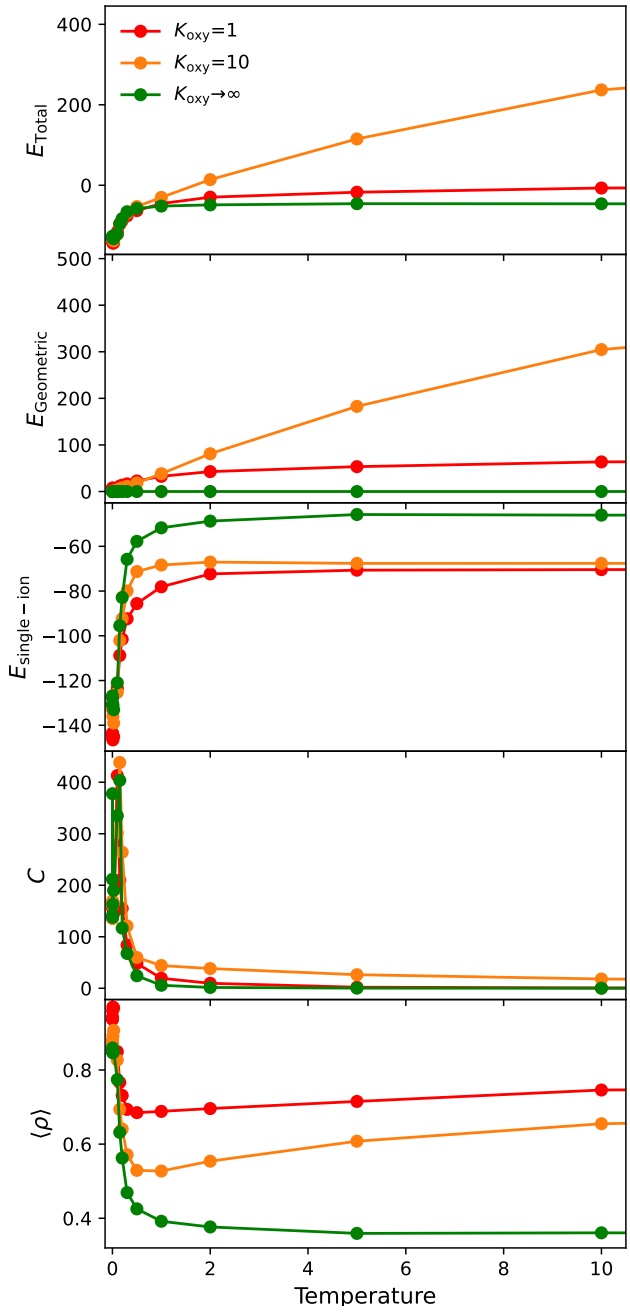

FIG. S14: The mean energy terms E_{total}, $E_{\text{Geometric}}$ (Eq 5), and $E_{\text{single-ion}}$ (Eq 2), heat capacity C, and mean $\langle\rho\rangle$, averaged over the final 10% of iterations in Monte Carlo simulations, as a function of temperature for the 10×30 nickelate lattice. The Monte Carlo simulations ran for 10^7 iterations in total at each temperature. We present these results as a function of the strength of the oxygen under-bonding penalty K_{oxy}. The corresponding figure with a logarithmic temperature scale is presented in Figure 7.

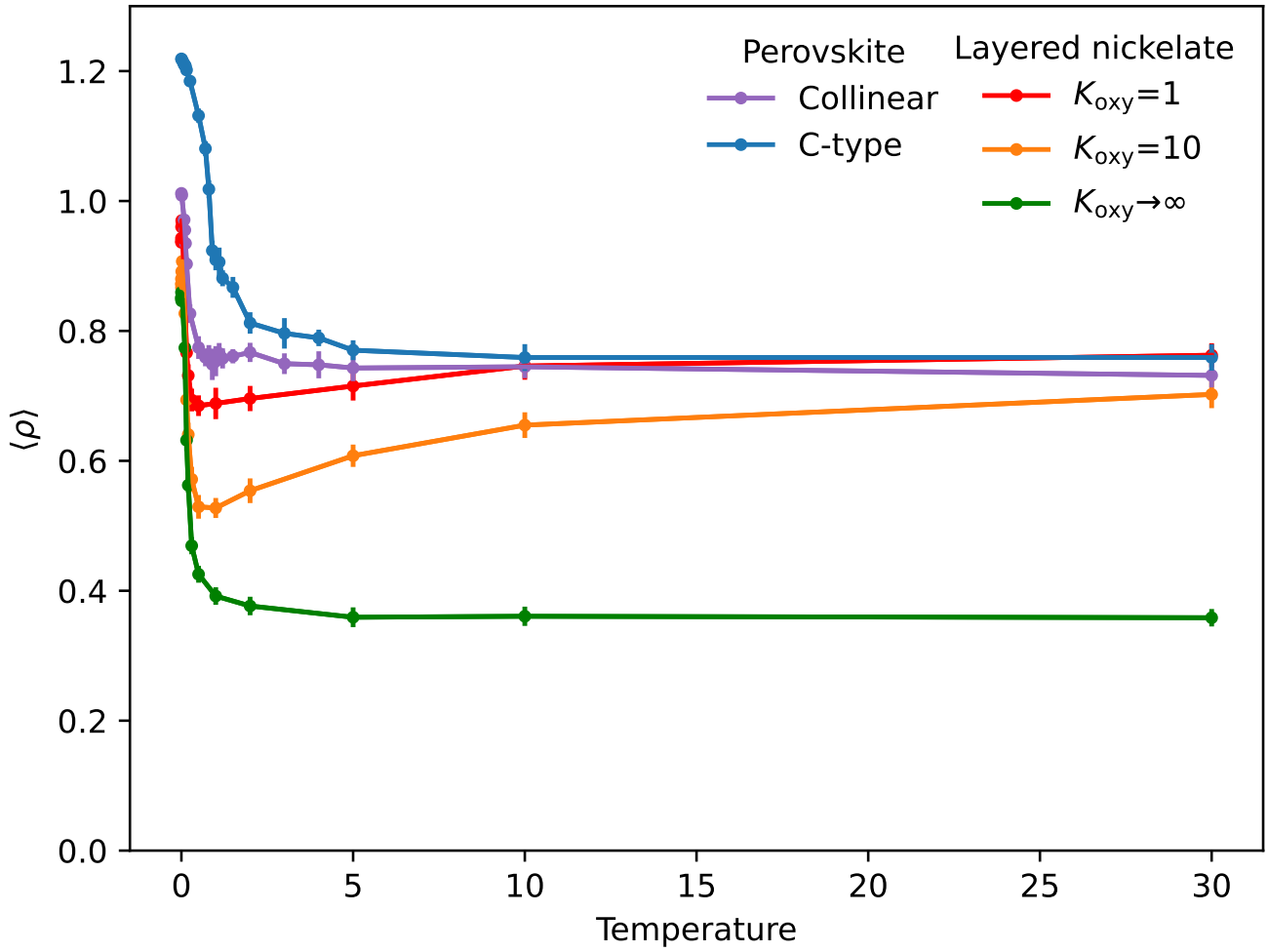

FIG. S15: $\langle\rho\rangle$ with temperature, comparing phase 1 (collinear) and phase 5 (C-type) perovskite ordering with layered nickelates for various K_{oxy}. The corresponding figure with a logarithmic temperature scale is Figure 8.

S4. Variable-size testing for perovskite cells

To test the impact of supercell size on the results (and ensure the resilience of our findings using the $8\times8\times8$ supercell with the perovskite structure) we also performed measurements using supercells with edge size 4 and 6. Figures S16 and S17 show the variable-temperature energy, heat capacity, and $\langle\rho\rangle$ for $4\times4\times4$ and $6\times6\times6$ supercells, respectively.

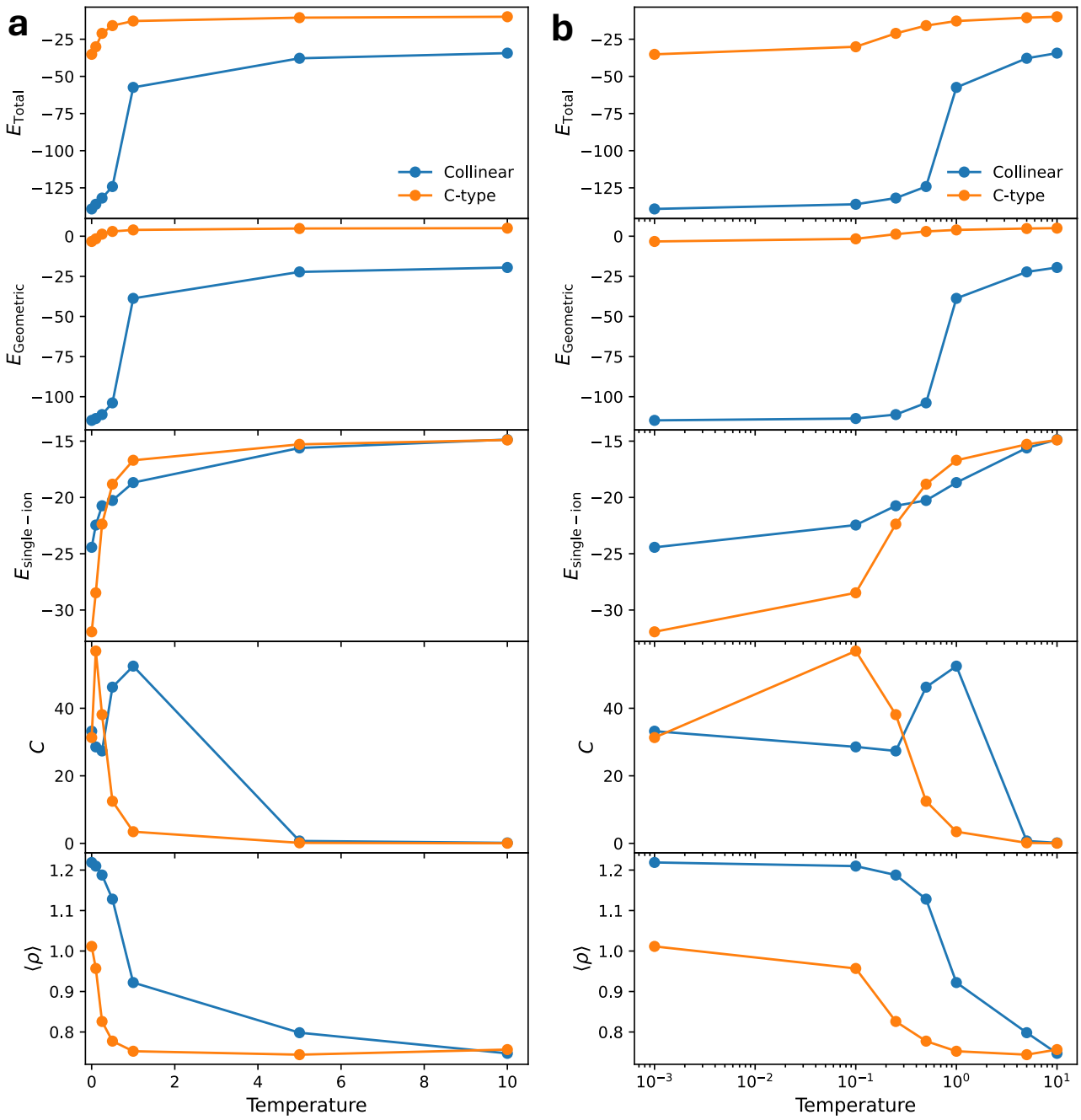

FIG. S16: Energy terms, $\langle\rho\rangle$, and C with temperature, averaged over the final 10% of iterations in Monte Carlo simulations, as a function of temperature for the collinear and C-type orbital orderings in a $4 \times 4 \times 4$ perovskite lattice. Each run lasted for 10^7 iterations. Data are plotted with temperature on a (a) non-logarithmic and (b) logarithmic scale.

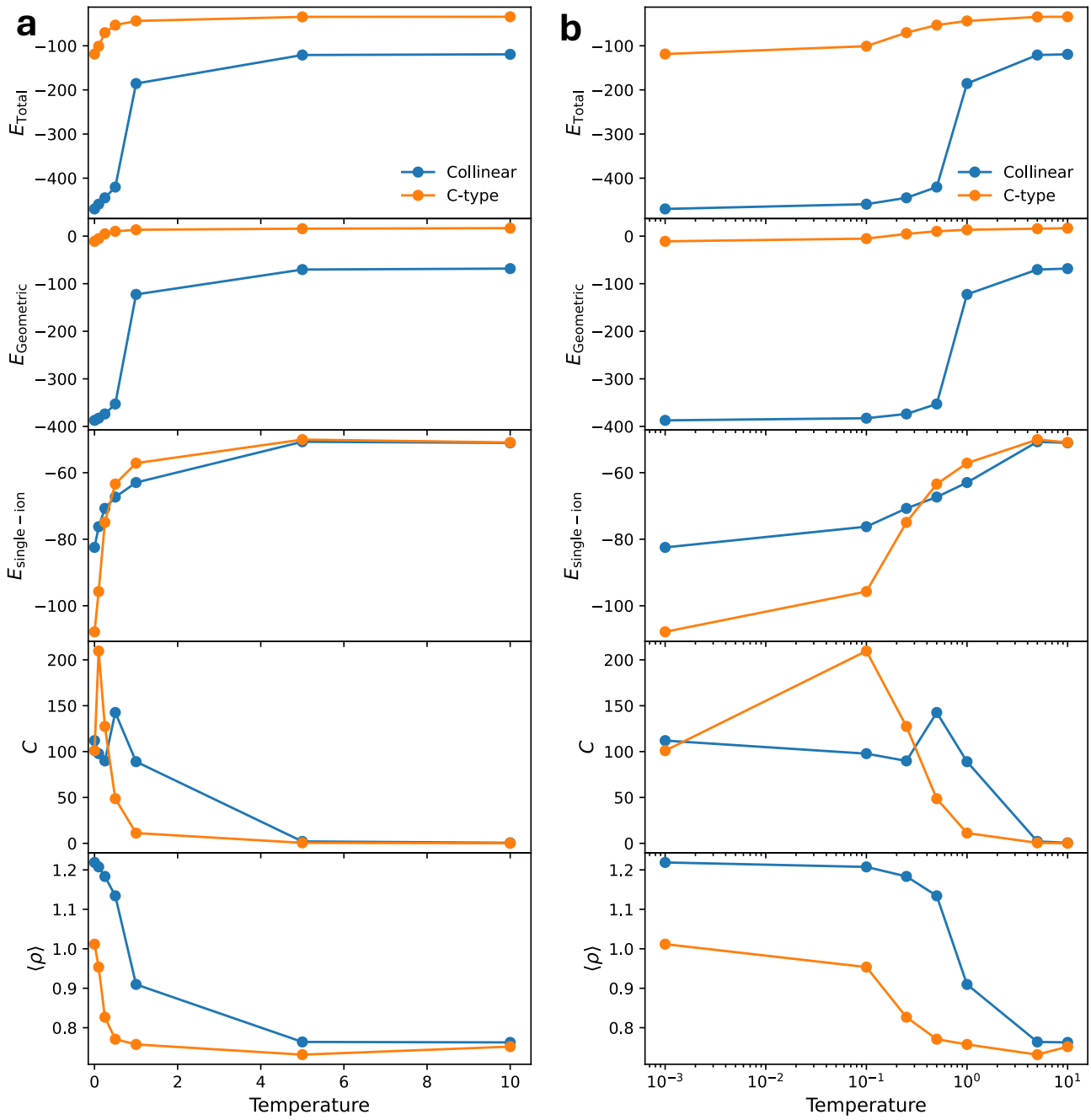

FIG. S17: Energy terms, $\langle\rho\rangle$, and C with temperature, averaged over the final 10% of iterations in Monte Carlo simulations, as a function of temperature for the collinear and C-type orbital orderings in a $6 \times 6 \times 6$ perovskite lattice. Each run lasted for 10^7 iterations. Data are plotted with temperature on a (a) non-logarithmic and (b) logarithmic scale.

S5. Histograms of ρ in final configuration

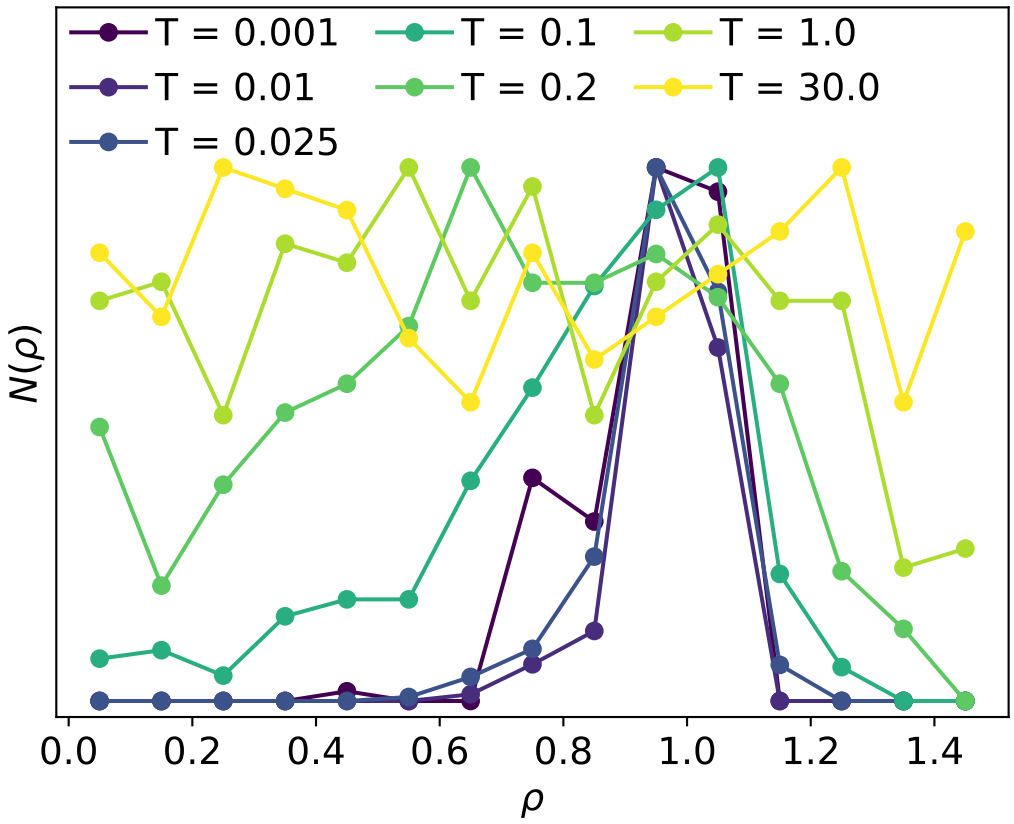

FIG. S18: Final histogram, after 10^7 iterations, of ρ distribution for layered nickelate with $K_{\text{oxy}} = 1$, at a selection of temperatures. The cell here was a single 10×30 nickelate layer.

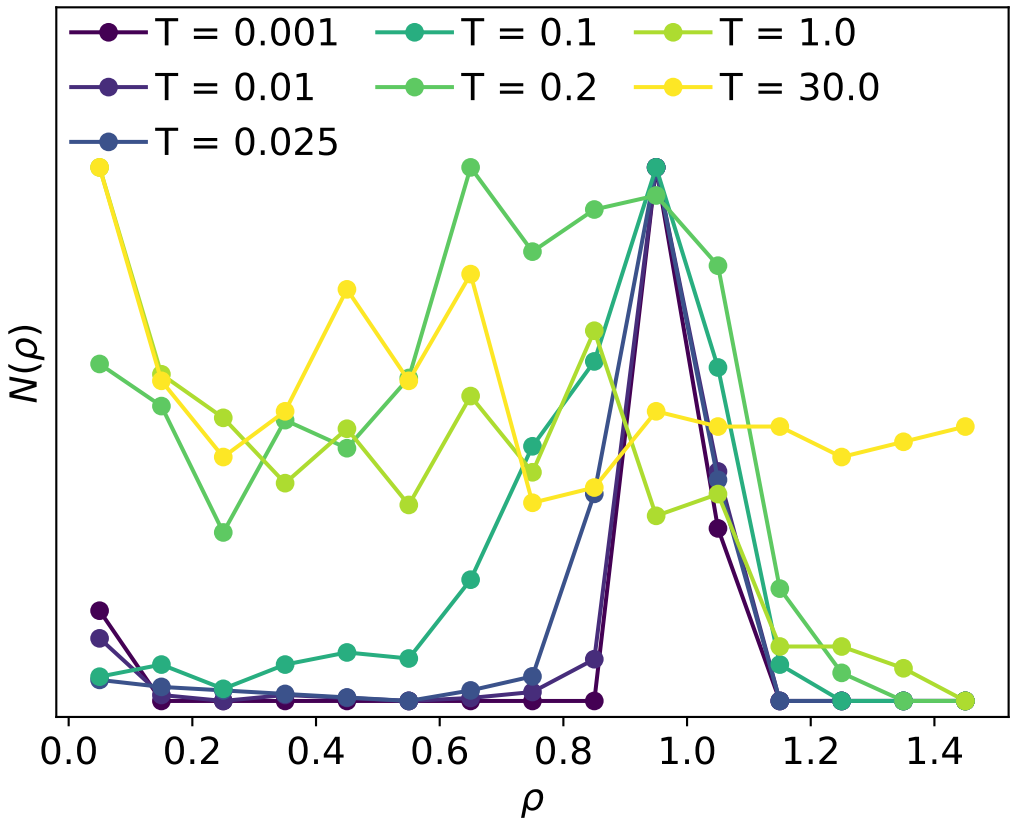

FIG. S19: Final histogram, after 10^7 iterations, of ρ distribution for layered nickelate with $K_{\text{oxy}} = 10$, at a selection of temperatures. The cell here was a single 10×30 nickelate layer.

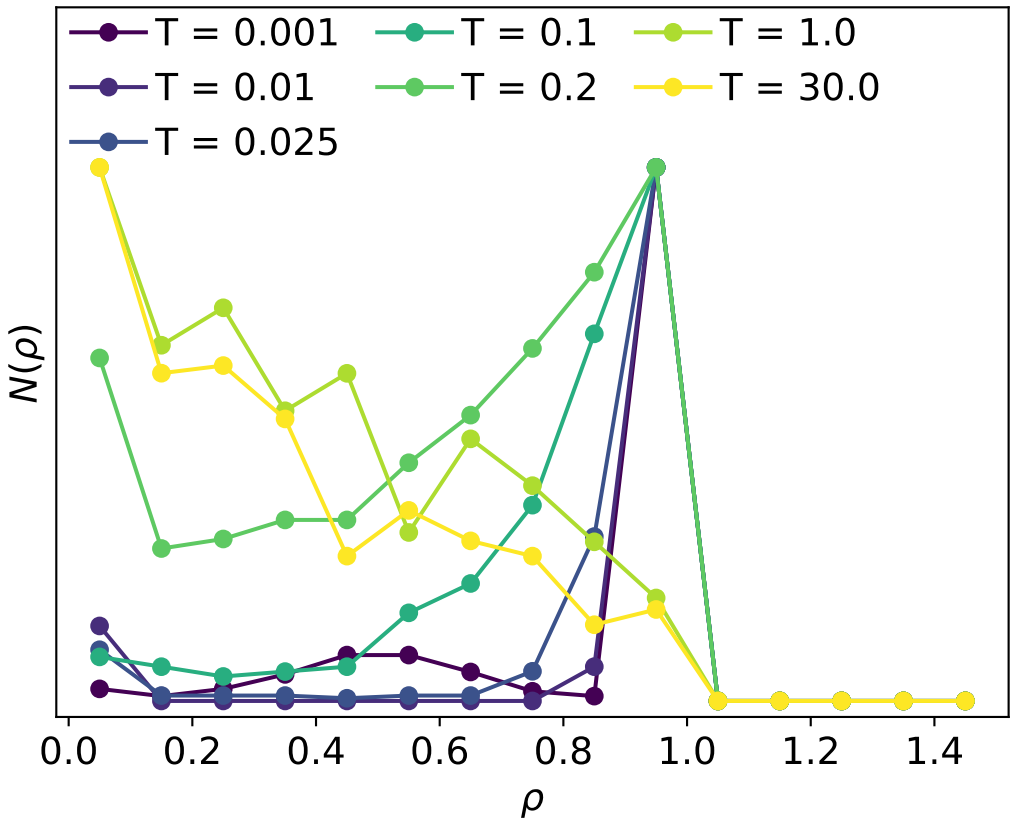

FIG. S20: Final histogram, after 10^7 iterations, of ρ distribution for layered nickelate with $K_{\text{oxy}} \to \infty$, at a selection of temperatures. The cell here was a single 10×30 nickelate layer.

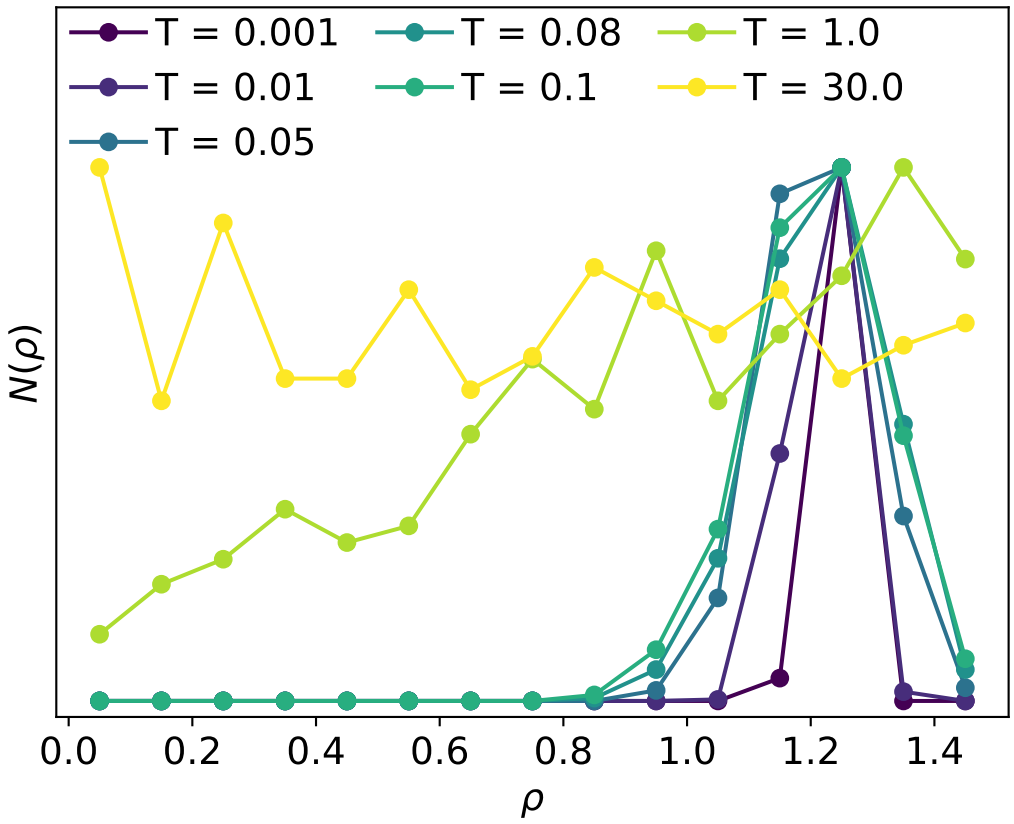

FIG. S21: Final histogram, after 10^7 iterations, of ρ distribution for $8 \times 8 \times 8$ phase 1 (collinear) perovskite, at a selection of temperatures.

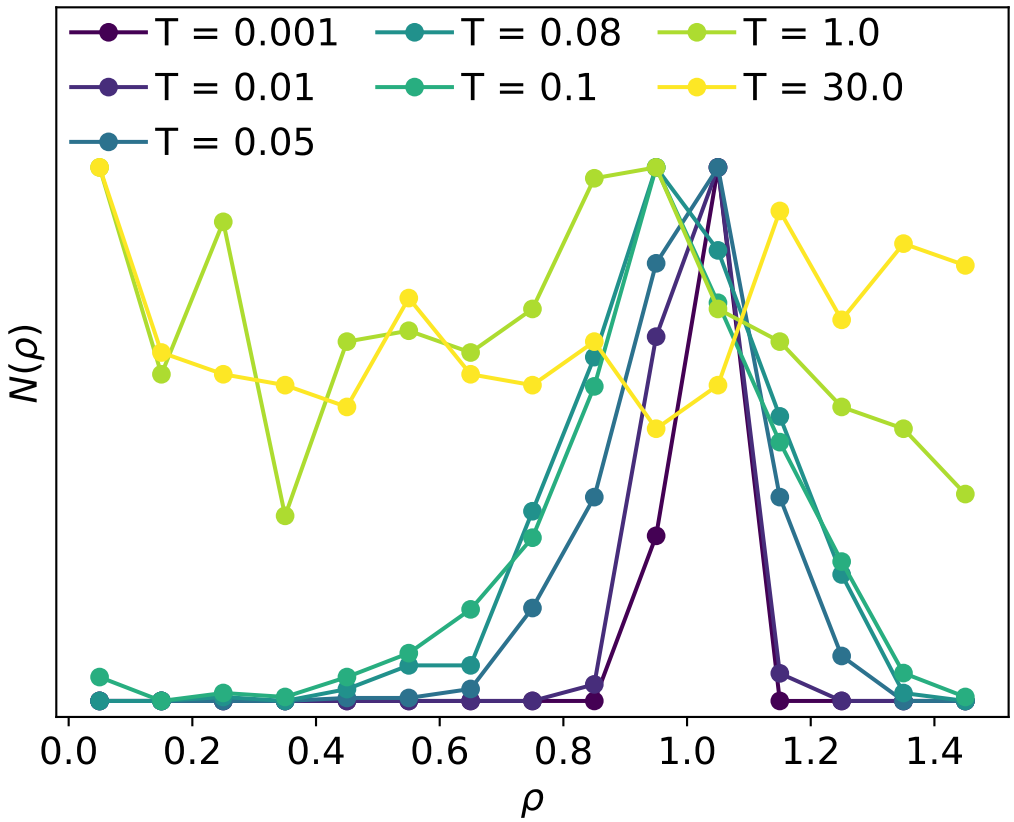

FIG. S22: Final histogram, after 10^7 iterations, of ρ distribution for $8 \times 8 \times 8$ phase 5 (C-type) perovskite, at a selection of temperatures.